



EUROPEAN ORGANISATION FOR NUCLEAR RESEARCH

CERN-EP/90-48

April 11, 1990

# A Measurement of Global Event Shape Distributions in the Hadronic Decays of the $Z^0$

The OPAL Collaboration

M.Z. Akrawy<sup>11</sup>, G. Alexander<sup>21</sup>, J. Allison<sup>14</sup>, P.P. Allport<sup>5</sup>, K.J. Anderson<sup>8</sup>, J.C. Armitage<sup>6</sup>, G.T.J. Arnison<sup>18</sup>, P. Ashton<sup>14</sup>, G. Azuelos<sup>16,J</sup>, J.T.M. Baines<sup>14</sup>, A.H. Ball<sup>15</sup>, J. Banks<sup>14</sup>, G.J. Barker<sup>11</sup>, R.J. Barlow<sup>14</sup>, J.R. Batley<sup>5</sup>, J. Becker<sup>9</sup>, T. Behnke<sup>7</sup>, K.W. Bell<sup>18</sup>, G. Bella<sup>21</sup>, S. Bethke<sup>10</sup>, O. Biebel<sup>3</sup>, U. Binder<sup>9</sup>, I.J. Bloodworth<sup>1</sup>, P. Bock<sup>10</sup>, H. Breuker<sup>7</sup>, R.M. Brown<sup>18</sup>, R. Brun<sup>7</sup>, A. Buijs<sup>7</sup>, H.J. Burckhart<sup>7</sup>, P. Capiluppi<sup>2</sup>, R.K. Carnegie<sup>6</sup>, A.A. Carter<sup>11</sup>, J.R. Carter<sup>5</sup>, C.Y. Chang<sup>15</sup>, D.G. Charlton<sup>7</sup>, J.T.M. Chrin<sup>14</sup>, I. Cohen<sup>21</sup>, W.J. Collins<sup>5</sup>, J.E. Conboy<sup>13</sup>, M. Couch<sup>1</sup>, M. Coupland<sup>12</sup>, M. Cuffiani<sup>2</sup>, S. Dado<sup>20</sup>, G.M. Dallavalle<sup>2</sup>, P. Debu<sup>19</sup>, M.M. Deninno<sup>2</sup>, A. Dieckmann<sup>10</sup>, M. Dittmar<sup>4</sup>, M.S. Dixit<sup>17</sup>, E. Duchovni<sup>24</sup>, I.P. Duerdoth<sup>7,d</sup>, D. Dumas<sup>6</sup>, H. El Mamouni<sup>16</sup>, P.A. Elcombe<sup>5</sup>, P.G. Estabrooks<sup>6</sup>, E. Etzion<sup>21</sup>, F. Fabbri<sup>2</sup>, P. Farthouat<sup>19</sup>, H.M. Fischer<sup>3</sup>, D.G. Fong<sup>15</sup>, M.T. French<sup>18</sup>, C. Fukunaga<sup>22</sup>, A. Gaidot<sup>19</sup>, O. Ganel<sup>24</sup>, J.W. Gary<sup>10</sup>, J. Gascon<sup>16</sup>, N.I. Geddes<sup>18</sup>, C.N.P. Gee<sup>18</sup>, C. Geich-Gimbel<sup>3</sup>, S.W. Gensler<sup>8</sup>, F.X. Gentit<sup>19</sup>, G. Giacomelli<sup>2</sup>, V. Gibson<sup>5</sup>, W.R. Gibson<sup>11</sup>, J.D. Gillies<sup>18</sup>, J. Goldberg<sup>20</sup>, M.J. Goodrick<sup>5</sup>, W. Gorn<sup>4</sup>, D. Granite<sup>20</sup>, E. Gross<sup>24</sup>, P. Grosse-Wiesmann<sup>7</sup>, J. Grunhaus<sup>21</sup>, H. Hagedorn<sup>9</sup>, J. Hagemann<sup>7</sup>, M. Hansroul<sup>7</sup>, C.K. Hargrove<sup>17</sup>, J. Hart<sup>5</sup>, P.M. Hattersley<sup>1</sup>, M. Hauschild<sup>7</sup>, C.M. Hawkes<sup>7</sup>, E. Heflin<sup>4</sup>, R.J. Hemingway<sup>6</sup>, R.D. Heuer<sup>7</sup>, J.C. Hill<sup>5</sup>, S.J. Hillier<sup>1</sup>, C. Ho<sup>4</sup>, J.D. Hobbs<sup>8</sup>, P.R. Hobson<sup>23</sup>, D. Hochman<sup>24</sup>, B. Holl<sup>7</sup>, R.J. Homer<sup>1</sup>, S.R. Hou<sup>15</sup>, C.P. Howarth<sup>13</sup>, R.E. Hughes-Jones<sup>14</sup>, P. Igo-Kemenes<sup>10</sup>, H. Ihssen<sup>10</sup>, D.C. Imrie<sup>23</sup>, A. Jawahery<sup>15</sup>, P.W. Jeffreys<sup>18</sup>, H. Jeremie<sup>16</sup>, M. Jimack<sup>7</sup>, M. Jobes<sup>1</sup>, R.W.L. Jones<sup>11</sup>, P. Jovanovic<sup>1</sup>, D. Karlen<sup>6</sup>, K. Kawagoe<sup>22</sup>, T. Kawamoto<sup>22</sup>, R.G. Kellogg<sup>15</sup>, B.W. Kennedy<sup>13</sup>, C. Kleinwort<sup>7</sup>, D.E. Klem<sup>17</sup>, G. Knop<sup>3</sup>, T. Kobayashi<sup>22</sup>, T.P. Kokott<sup>3</sup>, L. Köpke<sup>7</sup>, R. Kowalewski<sup>6</sup>, H. Kreuzmann<sup>3</sup>, J. von Krogh<sup>10</sup>, J. Kroll<sup>8</sup>, M. Kuwano<sup>22</sup>, P. Kyberd<sup>11</sup>, G.D. Lafferty<sup>14</sup>, F. Lamarche<sup>16</sup>, W.J. Larson<sup>4</sup>, M.M.B. Lasota<sup>11</sup>, J.G. Layter<sup>4</sup>, P. Le Du<sup>19</sup>, P. Leblanc<sup>16</sup>, A.M. Lee<sup>15</sup>, D. Lellouch<sup>7</sup>, P. Lennert<sup>10</sup>, L. Lessard<sup>16</sup>, L. Levinson<sup>24</sup>, S.L. Lloyd<sup>11</sup>, F.K. Loebinger<sup>14</sup>, J.M. Lora<sup>15</sup>, B. Lora<sup>16</sup>, M.J. Losty<sup>17</sup>, J. Ludwig<sup>9</sup>, N. Lupu<sup>20</sup>, J. Ma<sup>4,b</sup>, A.A. Macbeth<sup>14</sup>, M. Mannelli<sup>7</sup>, S. Marcellini<sup>2</sup>, G. Maringer<sup>3</sup>, A.J. Martin<sup>11</sup>, J.P. Martin<sup>16</sup>, T. Mashimo<sup>22</sup>, P. Mättig<sup>7</sup>, U. Maur<sup>3</sup>, T.J. McMahon<sup>1</sup>, A.C. McPherson<sup>6,c</sup>, F. Meijers<sup>7</sup>, D. Menszner<sup>10</sup>, F.S. Merritt<sup>8</sup>, H. Mész<sup>17</sup>, A. Michelini<sup>7</sup>, R.P. Middleton<sup>18</sup>, G. Mikenberg<sup>24</sup>, D.J. Miller<sup>13</sup>, C. Milstene<sup>21</sup>, M. Minowa<sup>22</sup>, W. Mohr<sup>9</sup>, A. Montanari<sup>2</sup>, T. Mori<sup>22</sup>, M.W. Moss<sup>14</sup>, P.G. Murphy<sup>14</sup>, W.J. Murray<sup>5</sup>, B. Nellen<sup>3</sup>, H.H. Nguyen<sup>8</sup>, M. Nozaki<sup>22</sup>,

A.J.P. O'Dowd<sup>14</sup>, S.W. O'Neale<sup>7,c</sup>, B.P. O'Neill<sup>1</sup>, F.G. Oakham<sup>17</sup>, F. Odorici<sup>2</sup>, M. Ogg<sup>6</sup>,  
 H. Oh<sup>4</sup>, M.J. Oreglia<sup>8</sup>, S. Orito<sup>22</sup>, J.P. Pansart<sup>19</sup>, G.N. Patrick<sup>18</sup>, S.J. Pawley<sup>14</sup>, P. Pfister<sup>9</sup>,  
 J.E. Pilcher<sup>8</sup>, J.L. Pinfold<sup>24</sup>, D.E. Plane<sup>7</sup>, B. Poli<sup>2</sup>, A. Pouladdej<sup>6</sup>, T.W. Pritchard<sup>11</sup>,  
 G. Quast<sup>7</sup>, J. Raab<sup>7</sup>, M.W. Redmond<sup>8</sup>, D.J. Rees<sup>1</sup>, M. Regimbald<sup>16</sup>, K. Riles<sup>4</sup>, C.M. Roach<sup>5</sup>,  
 S.A. Robins<sup>11</sup>, A. Rollnik<sup>3</sup>, J.M. Roney<sup>8</sup>, S. Rossberg<sup>9</sup>, A.M. Rossi<sup>2,a</sup>, P. Routenburg<sup>6</sup>,  
 K. Runge<sup>9</sup>, O. Runolfsson<sup>7</sup>, S. Sanghera<sup>6</sup>, R.A. Sansum<sup>18</sup>, M. Sasaki<sup>22</sup>, B.J. Saunders<sup>18</sup>,  
 A.D. Schaile<sup>9</sup>, O. Schaile<sup>9</sup>, W. Schappert<sup>6</sup>, P. Scharff-Hansen<sup>7</sup>, H. von der Schmitt<sup>10</sup>,  
 S. Schreiber<sup>3</sup>, J. Schwarz<sup>9</sup>, A. Shapira<sup>24</sup>, B.C. Shen<sup>4</sup>, P. Sherwood<sup>13</sup>, A. Simon<sup>3</sup>, G.P. Siroli<sup>2</sup>,  
 A. Skuja<sup>15</sup>, A.M. Smith<sup>7</sup>, T.J. Smith<sup>1</sup>, G.A. Snow<sup>15</sup>, E.J. Spreadbury<sup>13</sup>, R.W. Springer<sup>15</sup>,  
 M. Sproston<sup>18</sup>, K. Stephens<sup>14</sup>, H.E. Stier<sup>9</sup>, R. Ströhmer<sup>10</sup>, D. Strom<sup>8</sup>, H. Takeda<sup>22</sup>,  
 T. Takeshita<sup>22</sup>, T. Tsukamoto<sup>22</sup>, M.F. Turner<sup>5</sup>, G. Tysarczyk-Niemeyer<sup>10</sup>, D. Van den plas<sup>16</sup>,  
 G.J. VanDalen<sup>4</sup>, G. Vasseur<sup>19</sup>, C.J. Virtue<sup>17</sup>, A. Wagner<sup>10</sup>, C. Wahl<sup>9</sup>, C.P. Ward<sup>5</sup>,  
 D.R. Ward<sup>5</sup>, J. Waterhouse<sup>6</sup>, P.M. Watkins<sup>1</sup>, A.T. Watson<sup>1</sup>, N.K. Watson<sup>1</sup>, M. Weber<sup>10</sup>,  
 S. Weisz<sup>7</sup>, N. Wermes<sup>10</sup>, M. Weymann<sup>7</sup>, G.W. Wilson<sup>7</sup>, J.A. Wilson<sup>1</sup>, I. Wingarter<sup>7</sup>,  
 V.-H. Winterer<sup>9</sup>, N.C. Wood<sup>13</sup>, S. Wotton<sup>7</sup>, B. Wucsch<sup>3</sup>, T.R. Wyatt<sup>14</sup>, R. Yaari<sup>24</sup>,  
 Y. Yang<sup>4,b</sup>, G. Yekutieli<sup>24</sup>, T. Yoshida<sup>22</sup>, W. Zeuner<sup>7</sup>, G.T. Zorn<sup>15</sup>,

<sup>1</sup>School of Physics and Space Research, University of Birmingham, Birmingham, B15 2TT, UK

<sup>2</sup>Dipartimento di Fisica dell' Università di Bologna and INFN, Bologna, 40126, Italy

<sup>3</sup>Physikalisches Institut, Universität Bonn, D-5300 Bonn 1, FRG

<sup>4</sup>Department of Physics, University of California, Riverside, CA 92521 USA

<sup>5</sup>Cavendish Laboratory, Cambridge, CB3 0HE, UK

<sup>6</sup>Carleton University, Dept of Physics, Colonel By Drive, Ottawa, Ontario K1S 5B6, Canada

<sup>7</sup>CERN, European Organisation for Particle Physics, 1211 Geneva 23, Switzerland

<sup>8</sup>Enrico Fermi Institute and Department of Physics, University of Chicago, Chicago Illinois 60637, USA

<sup>9</sup>Fakultät für Physik, Albert Ludwigs Universität, D-7800 Freiburg, FRG

<sup>10</sup>Physikalisches Institut, Universität Heidelberg, D-6900 Heidelberg, FRG

<sup>11</sup>Queen Mary and Westfield College, University of London, London, E1 4NS, UK

<sup>12</sup>Birkbeck College, London, WC1E 7HV, UK

<sup>13</sup>University College London, London, WC1E 6BT, UK

<sup>14</sup>Department of Physics, Schuster Laboratory, The University, Manchester, M13 9PL, UK

<sup>15</sup>Department of Physics and Astronomy, University of Maryland, College Park, Maryland 20742, USA

<sup>16</sup>Laboratoire de Physique Nucléaire, Université de Montréal, Montréal, Québec, H3C 3J7, Canada

<sup>17</sup>National Research Council of Canada, Herzberg Institute of Astrophysics, Ottawa, Ontario K1A 0R6, Canada

<sup>18</sup>Rutherford Appleton Laboratory, Chilton, Didcot, Oxfordshire, OX11 0QX, UK

<sup>19</sup>DPhPE, CEN Saclay, F-91191 Gif-sur-Yvette, France

<sup>20</sup>Department of Physics, Technion-Israel Institute of Technology, Haifa 32000, Israel

<sup>21</sup>Department of Physics and Astronomy, Tel Aviv University, Tel Aviv 69978, Israel

<sup>22</sup>International Centre for Elementary Particle Physics and Dept of Physics, University of Tokyo, Tokyo 113, and Kobe University, Kobe 657, Japan

<sup>23</sup>Brunel University, Uxbridge, Middlesex, UB8 3PH UK

<sup>24</sup>Nuclear Physics Department, Weizmann Institute of Science, Rehovot, 76100, Israel

<sup>a</sup>Present address: Dipartimento di Fisica, Università della Calabria, 87036 Rende, Italy

<sup>b</sup>On leave from Harbin Institute of Technology, Harbin, China

<sup>c</sup>Now at Applied Silicon Inc

<sup>d</sup>On leave from Manchester University

<sup>e</sup>On leave from Birmingham University

<sup>f</sup>and TRIUMF, Vancouver, Canada

(submitted to Z. für Physik C)

## Abstract

We present measurements of global event shape distributions in the hadronic decays of the  $Z^0$ . The data sample, corresponding to an integrated luminosity of about  $1.3 \text{ pb}^{-1}$ , was collected with the OPAL detector at LEP. Most of the experimental distributions we present are unfolded for the finite acceptance and resolution of the OPAL detector. Through comparison with our unfolded data, we tune the parameter values of several Monte Carlo computer programs which simulate perturbative QCD and the hadronization of partons. Jetset version 7.2, Herwig version 3.4 and Ariadne version 3.1 all provide good descriptions of the experimental distributions. They in addition describe lower energy data with the parameter values adjusted at the  $Z^0$  energy. A complete second order matrix element Monte Carlo program with a modified perturbation scale is also compared to our 91 GeV data and its parameter values are adjusted. We obtain an unfolded value for the mean charged multiplicity of  $21.28 \pm 0.04 \pm 0.84$ , where the first error is statistical and the second is systematic.

# 1 Introduction

The measurement of distributions which characterize hadronic event structure in  $e^+e^-$  annihilations allows a general check on the global consistency of Quantum Chromodynamics (QCD) to describe experimental data, because global event shape variables such as Thrust and Sphericity are sensitive to the distribution of quarks and gluons created in the  $e^+e^-$  annihilation process. The most important uncertainty which affects these consistency checks is the mechanism by which quarks and gluons become confined inside hadrons (fragmentation), for which there is not yet a theoretical description. As a consequence, QCD calculations do not directly predict the distribution of hadrons observed in an experiment. Instead, perturbation theory is incorporated into a Monte Carlo simulation program which is used to generate a parton state. A model for fragmentation is applied to these partons to obtain the hadron state which may be compared to the experimental measurements.

A number of Monte Carlo programs describing multi-hadronic event production in  $e^+e^-$  annihilations has been developed, each of which represents a specific application of perturbation theory to QCD in conjunction with a model for the parton fragmentation. It is important to include more than one Monte Carlo program in a comparison of QCD predictions with experimental data in order to establish which features of the Monte Carlo description may be attributed to universal aspects of QCD, common to all models, and which features depend on the details of a particular model.

In this paper, we present experimental measurements of distributions which characterize the global properties of multi-hadronic events in  $Z^0$  decays, using a large sample of events collected with the OPAL detector at LEP. Most of the distributions are unfolded for the finite acceptance and resolution of the OPAL detector. We compare our measurements to several QCD based Monte Carlo programs and optimize their parameter values. We compare the predictions of the optimized Monte Carlos to hadronic event shape distributions measured at lower c.m. energies at PEP and PETRA.

In section 2 we describe those parts of the OPAL detector which are relevant for our analysis. We describe the OPAL data sample and our event selection criteria. In section 3 we define the global event shape distributions which we use. Section 4 contains a description of the Monte Carlo programs which are compared to our data. The procedure for unfolding the experimental distributions is presented in section 5; the unfolded data are presented in section 6. Section 7 contains an exposition of our technique and results for the optimization of the Monte Carlo parameter values. The comparison of optimized Monte Carlo with the hadronic  $Z^0$  decay data is contained in section 8. In section 9 we extend this study to include  $e^+e^-$  annihilation data collected at lower c.m. energies by other experiments. Section 10 summarizes our results.

## 2 The OPAL Detector and Hadronic $Z^0$ Decay Sample

The data were recorded with the OPAL detector at the CERN  $e^+e^-$  collider LEP. The present analysis is based on the entire OPAL data sample collected in 1989, corresponding to an integrated luminosity of about  $1.3 \text{ pb}^{-1}$ .

The main features of the OPAL detector have already been described [1]. Here we will briefly mention those aspects which are relevant for this paper. The tracking of charged particles is performed with a large volume cylindrical drift chamber of the jet chamber type, which is 4 meters in length and 3.7 meters in diameter. It is enclosed by a solenoidal magnet which provides an axial field for the measurement of charged particle momenta. The jet chamber covers a polar angle range of  $|\cos\theta| < 0.92$  and records up to 159 space points for each charged track which traverses its volume. The time-of-flight (TOF) counter array contains 160 scintillator bars which surround the magnet coil in the barrel region of OPAL and covers the angular range  $|\cos\theta| < 0.82$ . Particles from the interaction point are recognized by their proper timing with respect to the beam collision time using this TOF array. The electromagnetic calorimeter has three parts: a cylindrical part outside the TOF array with 9,440 lead glass blocks, 25 radiation lengths in depth, covering the angular range  $|\cos\theta| < 0.82$ , and two endcap parts with 1,132 blocks each, 20 radiation lengths in depth, covering the angular range from  $0.81 < |\cos\theta| < 0.98$ . The total solid angle coverage of the electromagnetic calorimeter is 98% of  $4\pi$ .

The data acquisition system was triggered if at least one of the following conditions was fulfilled: (1) the energy deposited in the electromagnetic calorimeter exceeded 6 GeV; (2) there was a signal in at least three non-adjacent scintillator bars in the time-of-flight system; (3) there were at least two charged tracks detected by a trigger logic utilizing the jet chamber information, for which both tracks had a transverse momentum greater than 450 MeV/c with respect to the beam axis and pointed toward the vicinity of the collision point. An on-line event filter [2] using the lead glass and time-of-flight information selected hadronic  $Z^0$  decay candidates. The combined trigger and selection efficiencies ( $97 \pm 0.6\%$ ) and the residual background from tau pairs, two-photon processes, beam-pipe interactions and cosmic radiation ( $< 1\%$ ) have been determined by various methods which are described in [3]. In total we obtained 29,197 multi-hadronic event candidates, which were next processed off-line through the full event reconstruction programs.

For the present analysis, we examine these multi-hadronic event candidates in two studies: one employs depositions of energy in the electromagnetic calorimeter ("clusters") and one employs charged tracks reconstructed in the jet chamber. By performing the analysis using these two independent measures of our multi-hadronic sample, we obtain the means to verify the consistency of the measurements and to establish that they are free of significant systematic bias. In particular we are able to establish that any deviations of Monte Carlo prediction from data are not due to imperfections in the simulation of the OPAL detector response, by studying our data in this manner. We applied additional selection criteria to the sample of 29,197 multi-hadronic events in order to obtain well contained events for each of the two cases.

For the study based on electromagnetic clusters, we used clusters which had an energy larger than 100 MeV for those in the barrel part of the calorimeter or 300 MeV for those in the endcap part of the calorimeter. In addition, we required that the clusters be associated with more than a single lead glass block. We next required that the thrust axis of an event, defined using the accepted clusters, lie more than 30 degrees in polar angle away from the beam axis. After applying this cut we obtained an event sample of 24,511 events.

For the study based on charged tracks, we required that at least five well reconstructed tracks be present in the event, where a well reconstructed track had at least 20 measured space points, a transverse momentum and polar angle with respect to the beam axis of at least 150 MeV/c and 20 degrees, respectively, and an extrapolated distance of closest approach to the interaction point of less than 5 cm in the direction perpendicular to the beam axis. The subsequent selection and analysis used only those tracks which satisfied these criteria. We required that the transverse momentum balance  $P_{\perp bat.}$ , defined by  $P_{\perp bat.} = |\sum_i \vec{p}_{\perp i}| / \sum_i |\vec{p}_{\perp i}|$ , where the sums are over the transverse momenta  $\vec{p}_{\perp i}$  of particles with respect to the beam axis, satisfy  $P_{\perp bat.} < 0.40$ . A reconstructed track was occasionally assigned an unrealistically large momentum value, i.e. considerably larger than the beam energy (because of a small level of random noise in the jet chamber): our last cut eliminated events having such a track (less than 2 per cent of all events were so rejected). In total we obtained a sample of 21,402 events.

The data have been collected at center-of-mass (c.m.) energies between 88.28 and 95.04 GeV. For the global event shape distributions studied in this paper, the difference between these energies is unimportant and data from the different c.m. energies are merged. The Monte Carlo event samples which are compared to these data were generated with a c.m. energy value of 91.3 GeV, corresponding to the weighted mean of the energy of the events in the experimental sample.

### 3 Experimental Distributions

A large number of event shape variables have been developed in order to characterize the structure of multi-hadronic final states in  $e^+e^-$  annihilations. The event shape distributions which we study are the following:

1. Thrust,  $T$
2. Thrust major,  $T_{major}$
3. Thrust minor,  $T_{minor}$
4. Oblateness,  $O$
5. Sphericity,  $S$
6. Aplanarity,  $A$
7. The  $D$  variable

8. The 2nd Fox-Wolfram moment normalized to the 0th moment,  $(H_2/H_0)$ .
9.  $\ln(1/x_p)$ , with  $x_p = 2 \cdot |\vec{p}_i|/E_{c.m.}$
10. Charged track multiplicity,  $n_{ch}$ .

Distributions 1-4 are based on thrust variables. Thrust  $T$  [4] is given by the expression

$$T = \max \left( \frac{\sum_i |\vec{p}_i \cdot \hat{n}|}{\sum_i |\vec{p}_i|} \right) ; \quad (1)$$

$\hat{n}_{Thrust}$  is the axis  $\hat{n}$  for which equation 1 is satisfied and is taken to be the event axis. Narrow two jet events have  $T \approx 1$  while isotropic events have  $T \approx 0.5$ . The Thrust major value  $T_{major}$  equals expression (1) for directions  $\hat{n} = \hat{n}_{Tmajor}$  in the plane perpendicular to  $\hat{n}_{Thrust}$  and is a measure for three jet structure. In the analogous manner, the Thrust minor value  $T_{minor}$  is given by expression (1) evaluated for the direction  $\hat{n} = \hat{n}_{Tminor}$  perpendicular to both  $\hat{n}_{Thrust}$  and  $\hat{n}_{Tmajor}$ . The event plane is the plane defined by  $\hat{n}_{Thrust}$  and  $\hat{n}_{Tmajor}$ ; thus planar events have  $T_{minor} \approx 0$ . Oblateness  $O$  is the difference  $O = T_{major} - T_{minor}$ ; events which are symmetric around  $\hat{n}_{Thrust}$  have  $O \approx 0$ .

Distributions 5 and 6 are based on the momentum tensor  $S^{\alpha\beta}$  [5], which is defined by

$$S^{\alpha\beta} = \frac{\sum_i p_i^\alpha \cdot p_i^\beta}{\sum_i p_i^2} ; \quad \alpha, \beta = 1, 2, 3 \quad (2)$$

In this expression, the sum runs over all particles  $i$  in the event and  $\alpha$  and  $\beta$  label the Cartesian coordinates of the 3-momentum  $\vec{p}_i$ . The eigenvalues of  $S^{\alpha\beta}$  are denoted  $Q_1$ ,  $Q_2$  and  $Q_3$ , for which  $Q_1 < Q_2 < Q_3$  and  $Q_1 + Q_2 + Q_3 = 1$ . Sphericity  $S$  and Aplanarity  $A$  are given by

$$S = \frac{3}{2} \cdot (Q_1 + Q_2) \quad (3)$$

$$A = \frac{3}{2} \cdot Q_1 ; \quad (4)$$

$S \approx 0$  for narrow two jet events while  $S \approx 1$  for spherical events. Planar events have  $A \approx 0$ . Therefore  $S$  and  $A$  are related to  $T$  and to  $T_{minor}$ , respectively, but are quadratic in momentum and are thus more sensitive to the high momentum particles in an event than are these last two variables.

The  $D$  variable [6] (distribution 7) is based on the sphericity tensor  $\theta^{\alpha\beta}$  [7], which is the linear analog of the sphericity tensor:

$$\theta^{\alpha\beta} = \frac{\sum_i (p_i^\alpha \cdot p_i^\beta) / |\vec{p}_i|}{\sum_i |\vec{p}_i|} ; \quad \alpha, \beta = 1, 2, 3 \quad (5)$$

The eigenvalues  $\lambda_1$ ,  $\lambda_2$  and  $\lambda_3$  of the sphericity tensor are used to construct the  $D$  variable:

$$D = 27 \cdot (\lambda_1 \cdot \lambda_2 \cdot \lambda_3) ; \quad (6)$$

$D \approx 0$  for two jet and planar events and is a measure of four jet structure.



We include the 2nd Fox-Wolfram moment  $H_2$  [8] in our study. This distribution is normalized to the 0th moment  $H_0$ . The ratio of moments ( $H_2/H_0$ ) (distribution 8) is given by

$$(H_2/H_0) = \frac{1}{2} \cdot \frac{\sum_{i,j} |\vec{p}_i| |\vec{p}_j| \cdot (3 \cos^2 \theta_{ij} - 1)}{\sum_{i,j} |\vec{p}_i| |\vec{p}_j|} ; \quad (7)$$

$(H_2/H_0) \approx 1$  for two jet events. It differs from Thrust variables and from variables constructed from the momentum or sphericity tensors in that it contains no reference to an event axis.

We also examine the distribution

$$\ln(1/x_p), \quad \text{with } x_p = 2 \cdot |\vec{p}_i|/E_{c.m.} \quad (8)$$

and the charged track multiplicity distribution  $n_{ch}$ . (distributions 9 and 10). We do not unfold these two distributions for the effects of detector acceptance and resolution to allow a systematic check on our Monte Carlo parameter optimization method and on the QCD model descriptions.

## 4 QCD Monte Carlo Simulation Programs

We next describe the QCD based Monte Carlo models which we compare to our data. We have selected four such models: Jetset version 7.2 [9], Herwig version 3.4 [10], a second order matrix element Monte Carlo with a modified perturbation scale [6] [11] [12] and Ariadne version 3.1 [13]. The four Monte Carlo programs together represent a wide difference of approach with regard to their application of perturbation theory to QCD and with regard to their modeling of confinement.

In the following, we discuss our implementations of these Monte Carlos and describe the adjustable parameters which control the momentum space distribution of hadrons.

### 4.1 Jetset version 7.2

There are a large variety of options provided by Jetset for simulating the evolution and fragmentation of partons. We choose the default option, by which the original quark-antiquark pair created in  $e^+e^-$  annihilation initiates a parton shower based on a leading logarithmic coherent branching formalism [14] and by which the transition to hadrons occurs according to the Lund string model for fragmentation [15]. Jetset incorporates a procedure by which the first gluon branching in the leading logarithmic shower is mapped onto the first order matrix element distribution for  $e^+e^- \rightarrow q\bar{q}g$ . This feature is intended to compensate for the unreliable description provided by the leading logarithmic approximation for the rate of hard, acolinear gluon emissions. An option of Jetset which we change from default is to allow photon emission from the quarks and antiquarks in the parton shower (final-state QED radiation). This final-state radiation is not important for the multi-hadronic event shape distributions which we study, however.

The main parameters of Jetset which control the momentum distributions of hadrons are listed in table 1. The parameter  $\Lambda_{QCD}$  is the QCD scale parameter, whose value determines the extent to which partons will branch;  $Q_0$  specifies the minimum mass-squared value to which partons may evolve and it serves to terminate the shower. The three parameters  $\sigma_q$ ,  $a$  and  $b$  belong to the fragmentation phase:  $\sigma_q$  controls the transverse momentum spectrum of hadrons with respect to the underlying string directions while  $a$  and  $b$  control the fragmentation function, or longitudinal momentum spectrum of hadrons, also with respect to the underlying string directions [15]. For our parameter optimization (section 7) we do not consider variation of the  $b$  parameter because its value is strongly correlated with that of  $a$ : it is generally sufficient to consider variation of either one or the other of these two parameters. Other fragmentation parameters are maintained at their default values.

The electroweak formalism in Jetset is based on the first order results of [16]. As such, the radiation of at most one initial-state photon is possible. The absence of higher order electroweak processes has no important consequences for the study of the global structure of multi-hadronic events in  $Z^0$  decay as is considered in this paper.

## 4.2 Herwig version 3.4

Like Jetset, Herwig is a parton shower Monte Carlo based on a leading logarithmic coherent branching formalism and with a model for parton fragmentation. Herwig contains a very detailed simulation for the parton shower phase, while implementing a simple scheme for fragmentation. Herwig includes the interference between partons due to parton spin, to the full leading logarithmic level [17], for example; it does not contain a mechanism to match the parton level distribution to the 3-jet matrix element in its general shower environment, however. Fragmentation is performed by associating partons at the end of the perturbative phase into colorless objects called clusters which then decay into two hadrons whose identity is determined by the available phase space [18].

The main parameters of Herwig for the control of the momentum distributions of hadrons are given in table 2. The QCD scale parameter  $\Lambda_{QCD}$  specifies the likelihood for branching in the shower;  $m_g$  is a formal mass value assigned to the gluon. In conjunction with the quark masses (whose values were left unchanged),  $m_g$  serves to terminate the perturbative evolution. The parameter  $M_{max}$  is a threshold parameter which determines whether a large mass cluster will evolve through a string-like mechanism to lower mass clusters rather than decay to hadrons directly.

Herwig contains only the Born level electroweak cross section describing quark pair creation and so does not permit the emission of an initial-state photon. Therefore we use Jetset to generate the initial  $q\bar{q}(\gamma)$  system, for the Herwig implementation (this is relevant only for the event samples which include simulation of the OPAL detector). The  $q\bar{q}$  system so obtained is used to initiate a parton shower according to the Herwig algorithm. At the end of the parton shower, the partons combine to form clusters which then decay to hadrons, again following the Herwig scheme. The simulation of the decays of these primary hadrons is performed using Jetset (version 7.2) rather than Herwig, however, because the decay tables

and decay algorithms of the former model are generally more complete and in better agreement with experiment than those of the latter. Thus the Jetset and Herwig models which we employ are identical in their descriptions of the electroweak scattering and of the decays of hadrons.

### 4.3 Ariadne version 3.1

Like Jetset and Herwig, Ariadne is based on the simulation of a parton shower. Ariadne differs from these leading logarithm models, however, in that gluon radiation is expressed as coherent emission from a parton system, or color dipole [19], rather than as independent emission from a single parton  $q \rightarrow qg$  or  $g \rightarrow gg$ .

The dipole formulation of gluon radiation incorporates interference phenomena into the perturbative framework (azimuthal correlations between partons, reduction of emission probability for soft gluons, etc.) in a manner which is considerably less complex than is the case for Jetset or Herwig. In the dipole scheme the kinematics of the parton branchings are given by Lorentz covariant expressions, again an advantage relative to the leading logarithm based programs. Because gluon emission is expressed as radiation from a parton system, the 1st order matrix element distribution for  $e^+e^- \rightarrow q\bar{q}g$  is incorporated into Ariadne in an integral and natural way. Furthermore, Ariadne treats interference for the case of hard gluon emissions, in addition to that of soft gluon emissions. The fragmentation of partons and decay of hadrons in Ariadne31 are performed using Jetset version 7.1 which is identical to Jetset version 7.2 for these two mechanisms.

The parameters which most affect the predictions of Ariadne for multi-hadronic event structure are listed in table 3. The parameters  $\Lambda_{QCD}$  and  $P_T^{min}$  control the perturbative phase; the parameters  $\sigma_q$ ,  $a$  and  $b$  belong to the Jetset fragmentation ansatz and have the same meaning as the corresponding parameters in table 1. The options of Ariadne which control dipole evolution, such as the functional form of the variable which terminates shower development, are left with the default definitions provided by the authors.

### 4.4 The ERT Matrix Element with a Modified Perturbation Scale

The matrix element program which we use is that of Magnussen [12], whose work is based upon the results of Ali and Barreiro [11]. This implementation of the 2nd order differential expressions of Ellis, Ross and Terrano [6] incorporates the scale  $\mu^2 = k \cdot E_{c.m.}^2$  ( $k < 1$ ) at which the strong coupling constant  $\alpha_S(\mu^2)$  is evaluated. Use of this modified scale leads to a better description of multi-jet rates in  $e^+e^-$  annihilations, by second order QCD matrix element Monte Carlos, than does use of the non-modified scale  $\mu^2 = E_{c.m.}^2$  [12][20].

It is necessary in the Monte Carlo treatment of matrix element calculations to impose finite jet resolution criteria, by which four parton states which fail certain cuts are reassigned to the two or three parton event categories. For our case, any two partons  $i$  and  $j$  with

invariant mass  $m_{ij}$  which satisfies

$$m_{ij}^2 < y_{min} \cdot E_{c.m.}^2 \quad (9)$$

are combined into one, where  $y_{min}$  is a cutoff parameter. There is some ambiguity in the manner by which the 4-momenta of the two partons should be combined: the Magnussen program uses the “ $E_0$  recombination” procedure [12] and so we refer to this Monte Carlo as “ERT-E0.” The ERT-E0 Monte Carlo uses Jetset, version 6.3, to describe parton fragmentation and hadron decay.

The main parameter values of ERT-E0 which are relevant to our study are listed in table 4:  $y_{min}$  and  $k$  have been discussed above;  $\Lambda_{\overline{MS}}$  is the QCD scale parameter in the  $\overline{MS}$  renormalization scheme while  $\sigma_q$ ,  $a$  and  $b$  are the Lund fragmentation parameters. We use the symmetric Lund fragmentation function [15] for all five quark species  $d$ ,  $u$ ,  $s$ ,  $c$  and  $b$ . The parameter values listed in the “Default Value” column of table 4 were obtained through comparisons with  $e^+e^-$  multi-hadronic annihilation data at c.m. energies of 35 and 44 GeV [12]. For our parameter adjustment we set the value of  $y_{min}$  to 0.01 as recommended in [21] and employ the values for  $k$  and  $\Lambda_{\overline{MS}}$  given in [12].

## 5 The Unfolding Procedure

To unfold the measured distributions for the effects of finite detector resolution and acceptance, we employ bin-by-bin correction constants. To determine these constants, a distribution is generated in the form of a histogram for two Monte Carlo samples: a sample (I) with no detector simulation and a sample (II) using the same Monte Carlo but including detector simulation and initial-state radiation. The events of sample (II) are subjected to the same reconstruction algorithms and event selection criteria as are the real data. The Monte Carlo sample (I) treats all particles with lifetimes greater than  $3 \cdot 10^{-10}$  s as stable particles and includes all stable charged and neutral particles including neutrinos and neutrons. Let  $U_i^{M.C.}$  be the number of entries in bin  $i$  of a distribution and  $N_U^{M.C.}$  be the number of events generated, for sample (I). Let  $D_i^{M.C.}$  and  $N_D^{M.C.}$  be the number of entries in histogram bin  $i$  and the number of events which survive after event reconstruction and selection, for sample (II). The correction factor  $C_i$  for bin  $i$  is then

$$C_i = \frac{(U_i^{M.C.}/N_U^{M.C.})}{(D_i^{M.C.}/N_D^{M.C.})} \quad (10)$$

This factor multiplies the number of entries  $D_i$  measured experimentally, for bin  $i$  of the distribution, to give the unfolded experimental value  $U_i$ :

$$U_i = C_i \cdot D_i \quad (11)$$

It is important that the Monte Carlo with detector simulation and initial-state radiation provide a good description of the distribution at the detector level, for this technique to be applicable.

The OPAL detector simulation program [22] is based on the GEANT3 package [23] developed at CERN. It simulates the effects of energy loss, bremsstrahlung, Compton scattering, multiple scattering, delta-ray production, pair production, hadronic interactions, photoelectric interactions and positron annihilation on the Monte Carlo particles which are tracked through a detailed model of the OPAL detector. As an end result we obtain Monte Carlo events in the same format as the experimental events collected with our data acquisition system.

We now discuss the bin-by-bin correction procedure as it relates to our analysis. In principle, a bin-by-bin correction procedure is justified when it is a good approximation to unfolding with a matrix [24]:

$$U = A \cdot D \tag{12}$$

where  $D$  and  $U$  are vectors. The vector  $D$  represents the distribution as it is determined directly from experimental data ("detector level"); the vector  $U$  represents the unfolded distribution;  $A$  is the matrix which relates them. Finite resolution implies that an element which appears in a certain bin of a histogram at the detector level may appear in a different bin at the unfolded level, thus that a bin-to-bin migration may occur in passing between the two levels. A bin-by-bin correction procedure is a good approximation to a matrix procedure when this bin-to-bin migration is small, which implies that the matrix  $A$  in (12) is approximately diagonal: that the bin widths have been adjusted to reflect the experimental resolution.

We determine the experimental resolution for a region of an event shape variable by generating Monte Carlo events, without detector simulation, having a value for that variable in the chosen region, and observing how much migration to other regions occurs when detector simulation and event selection are included. We define the resolution for a given region of a distribution to be the bin width which is necessary so that less than 40 per cent of the events migrate to other regions after inclusion of detector simulation and event selection. We obtain good representations of multi-hadronic event shape distributions measured by the calorimeter when detector simulation and initial-state radiation are included with the Monte Carlo predictions [25], making us confident that the resolution values which we derive are realistic reflections of the actual experiment.

In figure 1 we show the Thrust distribution as an illustration of how we select the histogram bin widths. We have determined the resolution for this distribution to be about 0.03 for the region above 0.90 using the definition of resolution given above. For figure 1 we generate the Thrust distribution using a bin width of 0.01 for  $T > 0.93$ , which is purposely chosen to be narrower than the resolution, and apply bin-by-bin corrections to a Monte Carlo sample of Herwig events which include initial-state radiation and which have been processed through our detector simulation program. The correction factors are determined using Jetset with our optimized parameter values (section 7). The points with error bars in figure 1 indicate the unfolded Herwig events. The solid histogram shows the Herwig distribution obtained without initial-state radiation or detector simulation (generator level); the dashed histogram shows the corresponding distribution for Jetset. The unfolded Herwig values for the two highest bins ( $T > 0.98$ ) are biased toward the Jetset distribution, i.e. toward the Monte Carlo used to calculate the correction constants. This demonstrates that important biases can be introduced

into data by a bin-by-bin correction procedure. This bias can be especially important if the bin widths are much narrower than the experimental resolution [24]. For hadronic event shape distributions, this problem is particularly acute for regions which correspond to narrow two jet events where the distribution falls off rapidly in value, such as the Thrust region above 0.98. In contrast, no particular bias is introduced by the correction procedure for Thrust values between about 0.90 and 0.98 even though the bin widths are narrower than the resolution in this region as well. We conclude that certain regions of the event shape distributions may be binned rather narrowly, according to the experimental statistics rather than to the resolution, without introducing undue bias. These regions generally correspond to the central parts of the distributions.

To select the bin widths for the unfolded distributions, we therefore apply the type of analysis represented in figure 1 to identify those regions where the bin widths may be rather narrow compared to the resolution while avoiding the introduction of a bias as is discussed above. For those regions where a bias is apparent because the unfolded Herwig distribution lies systematically above or below the generator level Herwig distribution, we employ bin widths which equal the resolution values; otherwise we employ narrower bin widths. By selecting the bin widths in this manner, we keep the bias which is introduced by the unfolding procedure at a reasonably small level.

## 6 The Unfolded Data

To unfold our data, we use correction factors  $C_i$  determined from Jetset72, using the optimized parameter set (section 7). Jetset with these parameter values provides a good description of the event shape distributions we unfold when simulation of the detector and initial-state radiation are included, which makes it suitable for the calculation of  $C_i$ . The values of  $C_i$  which we obtain are between 0.80 and 1.20 for 106 of the 109 bins in the unfolded distributions; the largest value is for one bin of Aplanarity ( $C_i=1.41$ ). In addition a few bins of the distributions are not unfolded, such as the region of  $T_{minor}$  between 0.00 and 0.04, because of the largeness of the corrections which would be required. Thus the values of the corrections which are used to unfold the distributions are reasonably close to unity.

For some of the distributions there is a rather rapid change in the value of the correction constant between a bin and its neighbor. Such a situation holds for the first bin of Sphericity and Aplanarity and for the last bin of Thrust, for example (see figure 2). This situation occurs because the effect of the detector is to migrate events towards the narrow two jet region, due to finite granularity in the calorimeter by which energy deposits in the core of a jet are merged. This effect does not introduce a bias of any significance into the unfolded measurements as we have determined through the study of bin widths discussed in section 5. Initial-state photon radiation, whose effects are also removed in the unfolding process, contributes about 5 per cent (or less) to the values of the bin-by-bin correction constants. The smallness of this contribution is because energetic initial-state photon radiation is suppressed by the  $Z^0$  pole.

We consider two sources of systematic error for the unfolded data values. The first of these accounts for residual Monte Carlo bias which remains despite the adjustment of histogram bin

widths to minimize this effect. To account for this residual bias, we assign a systematic error to each unfolded data point equal to the absolute value of the difference between the Herwig prediction for that bin with no initial-state radiation or detector simulation and the value of the Herwig distribution for that bin with initial-state radiation and detector simulation, which has been unfolded using the Jetset correction values. This corresponds to the difference between the points with error bars and the solid histogram in figure 1, for example, using the final bin width assignments. This method of assigning the systematic error to the measured data points thereby incorporates a direct measurement of the bias which is introduced by the unfolding process. The second source of systematic error which we consider is due to misrepresentation of the calorimeter measurements by the Monte Carlo. We study this by changing the representation of that detector in the detector simulation program and observing the effect on the unfolded measurements. The efficiency of light collection by the light guides, the difference in response of the different types of lead glass blocks and the amount of material between the collision point and the calorimeter were varied. In addition the neutron content in the Monte Carlo generator was varied by a factor of three in order to ascertain the importance on our correction values of an imprecise knowledge of the particle composition in  $Z^0$  decays. These studies demonstrate that the error due to detector misrepresentation or uncertainty in the particle composition is small compared to the other errors and we do not include them in our final error values.

In figures 2 (a)-(h) and in tables 5-12 we present our unfolded measurements of the multi-hadronic event shape distributions. The values of the correction constants  $C_i$  used to unfold the data are shown in the small inset above each distribution. Also shown in these figures are the predictions of the QCD Monte Carlos using their optimized parameter values. The difference between the Monte Carlo predictions and data points, in units of standard deviation, are shown in the small inset below each distribution.

The errors on the data points in figure 2 are a combination of the statistical and systematic errors on that quantity, added in quadrature. The statistical errors are derived through propagation of errors from equation (11) and include the statistical errors on the correction factor values. The statistical errors on the Monte Carlo curves in figure 2 are typically a factor of three to four less than the errors shown for the experimental data. In tables 5-12 the statistical and systematic errors are given separately.

## 7 Monte Carlo Optimization

An important factor in the determination of the “best” values for a phenomenological parameter set is the selection of the distributions to be employed for the parameter constraint. We adopt a simple scheme and optimize the parameter values of the QCD models using the  $T_{major}$  and  $(H_2/H_0)$  distributions only. The selection of these two distributions is suggested (1) because they are sensitive to variation of the main parameters for all four of the QCD models, (2) because the two distributions together do not constrain every degree-of-freedom for multi-hadronic event structure and (3) because they are generally well behaved with regard to the unfolding, cf. the correction factor values shown above figures 2 (b) and (h).

The distributions  $T_{major}$  and  $(H_2/H_0)$  together do not constrain particle multiplicity, nor do they completely constrain the other unfolded distributions which we examine: an event which has an intermediate value of  $T_{minor}$  can be in the two-jet region of  $(H_2/H_0)$  and  $T_{major}$  or very far from the two-jet region as measured by these two variables. Having adjusted the Monte Carlo to describe  $T_{major}$  and  $(H_2/H_0)$ , we will therefore be able to verify the global consistency of the QCD model descriptions by examining the model predictions for other distributions: the validity of this consistency check would be less transparent should the Monte Carlo parameters be adjusted using a set of distributions which constrains all degrees-of-freedom.

We next describe our Monte Carlo parameter optimization method, which contains two elements: (1) multi-parameter variation based on  $\chi^2$  values and (2) single parameter variation based on visual inspection of systematic trends. Element (1) is used for the coarse adjustment of parameter values, element (2) for the final adjustment.

We begin by examining the predictions of a Monte Carlo for the  $T_{major}$  and  $(H_2/H_0)$  distributions, using either default parameter values or parameter values determined from lower energy  $e^+e^-$  annihilation data. If the Monte Carlo sample so generated is in reasonable agreement with our measurements (which is true for Jetset and Ariadne), we skip to step (2) of the previous paragraph for final adjustment. If the model requires coarse adjustment (which is true for Herwig and the ERI-E0 Monte Carlo), we first apply an iterative multi-parameter fitting algorithm based on  $\chi^2$  values in order to achieve approximate agreement with the data. This multi-parameter fitting algorithm is based on a first order Taylor expansion of the predictions of a Monte Carlo in terms of the parameters being tuned, and follows the technique presented in ref. [26]. Monte Carlo studies have shown that this fitting algorithm finds the "correct" parameter values of a Monte Carlo, within reasonable limits, when Monte Carlo events are used as a toy data sample for which the correct parameter values are therefore known.

We use Herwig as an example of this model tuning method. The parameters whose variation are considered are  $\Lambda_{QCD}$ ,  $m_g$  and  $M_{max}$ , whose default values are given in table 2. We obtain  $\chi^2$  values of 97.5 (10 bins) and 109.3 (11 bins) between Herwig and the unfolded data, for  $T_{major}$  and for  $(H_2/H_0)$ , using this default set. For the multi-parameter fitting algorithm, we employ relatively small samples of 5,000-10,000 Monte Carlo events at each point of the parameter space in order to minimize computer time. Application of this algorithm results in the values  $\Lambda_{QCD} = 0.11$ ,  $m_g = 0.65$  and  $M_{max} = 2.2$  which give much better agreement with experiment:  $\chi^2 = 8.2$  for  $T_{major}$  and  $\chi^2 = 9.6$  for  $(H_2/H_0)$ . We next adjust the parameters one at a time, starting with these values and employing larger Monte Carlo statistics of 50,000 events at each point, to search visually for systematic improvements in the description of data. The final optimized parameter set for Herwig is  $\Lambda_{QCD} = 0.11$ ,  $m_g = 0.65$  and  $M_{max} = 3.00$  which leads to  $\chi^2$  values of 8.4 (10 bins) and 6.2 (11 bins) for the  $T_{major}$  and  $(H_2/H_0)$  distributions, respectively.

For Jetset we consider variation of the parameters  $\Lambda_{QCD}$ ,  $Q_0$ ,  $\sigma_q$  and  $a$ , whose default values are given in table 1. We begin not with these default values but with values which the TASSO collaboration found to give a good description of their data at  $E_{c.m.}=35$  GeV [27]:  $\Lambda_{QCD} = 0.26$ ,  $Q_0 = 1.0$ ,  $\sigma_q = 0.39$ ,  $a = 0.18$  and  $b = 0.34$ . Jetset with the TASSO parameters



also describes our data quite well [25]: we find  $\chi^2$  values, between Jetset72 and the unfolded distributions, of 10.1 (10 bins) and 13.8 (11 bins) for  $T_{major}$  and  $(H_2/H_0)$  using the TASSO parameter set. We thus proceed directly to final adjustment. The optimized parameter set for Jetset is  $\Lambda_{QCD} = 0.29$ ,  $Q_0 = 1.0$ ,  $\sigma_q = 0.37$  and  $a = 0.18$ . For this optimized set we obtain  $\chi^2$  values of 7.7 (10 bins) and 4.0 (11 bins) for the  $T_{major}$  and  $(H_2/H_0)$  distributions, respectively, when compared to the unfolded measurements.

In a similar manner, we obtain the values  $\Lambda_{QCD} = 0.20$ ,  $P_T^{min} = 1.0$  and  $\sigma_q = 0.37$  in an optimization of the Ariadne parameters (table 3) to the  $T_{major}$  and  $(H_2/H_0)$  histograms. We do not vary the parameters  $a$  and  $b$  in this instance but utilize the same values which are chosen for Jetset. The  $\chi^2$  values between the optimized Ariadne model and data are 7.1 (10 bins) for  $T_{major}$  and 5.0 (11 bins) for  $(H_2/H_0)$ .

Lastly, we present our optimized parameter set for the ERF-E0 model. For this Monte Carlo we have considered variation of the parameters  $\sigma_q$ ,  $a$  and  $b$  and find values of 0.52, 1.2 and 0.60, respectively. The  $\chi^2$  values between the ERF-E0 Monte Carlo and the unfolded data are 17.0 (10 bins) for  $T_{major}$  and 23.7 (11 bins) for  $(H_2/H_0)$ , compared to values 62.5 and 42.7 yielded by the default parameter set listed in table 4.

We next generated new Monte Carlo samples for Jetset and Herwig which included simulation of the detector, initial-state radiation and the optimized parameter values, from which the final corrections and systematic errors for the unfolded distributions (figure 2 and tables 5-12) were derived.

## 8 Comparison of Monte Carlos with 91 GeV Data

We next discuss the goodness-of-description of our 91 GeV data by the QCD models using the optimized parameter sets. We include not only the unfolded distributions presented in figure 2 but additional distributions employing the charged track based event sample.

From figure 2 it is seen that Jetset provides a good overall description of the unfolded distributions. Herwig also provides a good overall description, but its predictions lie systematically below the data in the low statistics tails of the Thrust,  $T_{major}$ , Oblateness and Sphericity distributions. This lowness of the Herwig predictions relative to the data is mostly encompassed within the systematic errors assigned to the measurements, however. If Herwig is used to calculate the correction constants instead of Jetset, the unfolded data points lie closer to the Herwig curves: it is the Jetset predictions which demonstrate a systematic deviation with the data in this case. We do not observe systematic differences between the Jetset and Herwig predictions when detector simulation and initial-state radiation are included. Both models yield an equally good description of the measured event shape distributions at this level. We conclude that the lowness of the Herwig predictions relative to the unfolded data, for the low statistics tails of the four distributions just mentioned, does not represent a discrepancy with our data. A residual bias toward Jetset is present for these tails because the bin widths in these regions cannot be so large as to prevent all migration into other regions when the effects of detector resolution are included (section 5): this residual bias is

accounted for by the errors which are assigned to the measurements. A possible source of the difference between the Jetset and Herwig curves in figure 2 is the 3-jet matrix element which is incorporated into the Jetset parton shower algorithm but which is lacking in that of Herwig. Inclusion of this feature in Herwig could result in a larger rate for hard, acollinear gluon bremsstrahlung thus bringing its predictions in the tails of distributions like Thrust and Sphericity closer to those of Jetset.

Ariadne also describes our measured distributions well. Generally speaking, its predictions for the shapes of the variables are quite similar to those of Jetset. At the parton level, the Jetset and Ariadne predictions for the event shape distributions are also very similar. This implies that the differences between the dipole and leading logarithm parton showers are not important for the global distributions which we study. Because of the similarity in the parton level distributions, we conclude that the similarity in the predictions of the two Monte Carlos at the hadron level is not due entirely to the reliance of Ariadne on Jetset for fragmentation.

The ERT-E0 model does not provide as good a description of the measurements as do the parton shower models. There are important discrepancies with data for the high statistics bins of Thrust and  $(H_2/H_0)$ , which correspond to two-jet-like regions, for example. The relatively poor description of these regions is presumably due to the lack of hard, somewhat collinear radiation in the matrix element treatment, related to the finite value of the cutoff parameter  $y_{min}$ . At the c.m. energy of 91 GeV, the value of 0.01 assigned to that parameter means that the minimum invariant mass for real parton emission is about 9 GeV/c<sup>2</sup>. The invariant mass region for real parton emission below 9 GeV/c<sup>2</sup> is therefore left unpopulated in the matrix element treatment. This gap is partially but not entirely filled by adjustment of the fragmentation parameters. The value 0.01 is close to the minimum which can be assigned to the parameter  $y_{min}$ : should its value be less than this, the probability for two jet production would become negative which is not physical. By including the two jet region along with the rest of the distribution for the parameter constraint (so as to treat all Monte Carlos in an equivalent manner), we force the ERT-E0 Monte Carlo to describe a region for which it is not suited. The ERT-E0 model also shows discrepancies with data in regions of distributions which can be associated with four jet production, such as the tails of  $T_{minor}$ , Aplanarity and the  $D$  variable, where its predictions are low relative to the measurements. Similar discrepancies of 2nd order matrix element Monte Carlos with 91 GeV data have been reported by the ALEPH [28] and DELPHI [29] collaborations, using parameter values which are adjusted to describe lower c.m. energy event samples. Certain regions of the distributions which are dominated by 3-jet production, such as the tail of the Thrust distribution, are reasonably well described by ERT-E0.

The  $\chi^2$  values between the Monte Carlo predictions and our unfolded measurements are given in table 13. These  $\chi^2$  values emphasize the good descriptions provided by the three parton shower models. By far the largest contributions to the overall  $\chi^2$  value of ERT-E0 are from the  $T_{minor}$  and Aplanarity distributions.

The predictions of the optimized QCD Monte Carlos for the charged multiplicity distribution  $n_{ch}$  provide an independent test of their consistency at describing multi-hadronic event structure at 91 GeV since the model optimization method (section 7) is based on comparison with the  $T_{major}$  and  $(H_2/H_0)$  distributions, neither of which are directly related to that quan-

tity. The Jetset and Herwig predictions for charged multiplicity are shown in comparison with the OPAL data in figure 3 (a). This distribution is not unfolded: therefore the Monte Carlo predictions include initial-state radiation and detector simulation. The description of this distribution is good by both Jetset and Herwig. Without detector simulation or initial-state radiation we obtain mean charged particle multiplicity values  $\langle n_{ch.} \rangle$  of 21.4 for Jetset, 21.2 for Herwig, 20.9 for Ariadne and 19.1 for ERT-E0, using the optimized parameter sets. These values may be compared to the OPAL measured value for the unfolded mean charged multiplicity:  $\langle n_{ch.} \rangle = 21.28 \pm 0.04 \pm 0.81$ , where the first error is statistical and the second is systematic. This measured value for  $\langle n_{ch.} \rangle$  has been obtained by applying a correction constant from Jetset which equals the ratio between that model's prediction for  $\langle n_{ch.} \rangle$  without detector simulation or initial-state radiation and its prediction for  $\langle n_{ch.} \rangle$  when these two effects are included. The systematic error includes the contribution from QCD model dependence (0.2 units), uncertainty in detector performance (0.5 units), uncertainty in the track reconstruction (0.7 units) and the uncertainty related to the track and event selection (0.1 units each). Our unfolded value for  $\langle n_{ch.} \rangle$  agrees well with those presented in [28] [29] [30]. The three parton shower models with their optimized parameters are in good agreement with the measured value for  $\langle n_{ch.} \rangle$  while the value provided by the matrix element model is somewhat low.

In figures 3 (b), (c) and (d) we present the  $T_{major}$ ,  $(H_2/H_0)$ , and  $\ln(1/x_p)$  distributions, measured with the charged track based event sample. For figures 3 (b) and (c) the particle momenta have been projected into the plane perpendicular to the beam axis to make use of the best momentum measurement. The distributions of figure 3 are not unfolded for detector effects or initial-state radiation allowing us to employ narrow bin widths based on the event statistics. The predictions of the optimized Herwig and Jetset models, including detector simulation and initial-state radiation, are also shown in figure 3. The charged track based distributions are well described by both Monte Carlos: in conjunction with the good descriptions provided by these Monte Carlos for the unfolded distributions of figure 2, this demonstrates the consistency between our measurements and the QCD model descriptions. From two independent experimental measurements, one from the electromagnetic calorimeter and one from the jet chamber, we thus establish a systematic check on our unfolded data and on the consistency of the QCD model descriptions. The  $\chi^2$  values yielded by Jetset and Herwig for the charged track based distributions are given in table 14.

## 9 Comparison with Lower Energy Data

An important test of the QCD models comes from comparing their predictions to data at different c.m. energies using the same parameter values. We next compare multi-hadronic event shape distributions measured by the MARK2 [31] and TASSO [27] collaborations at 29 GeV and 35 GeV, respectively, to the predictions of the QCD Monte Carlos which we have optimized to the OPAL data. We study the Thrust, Sphericity and Aplanarity distributions as these are standard event shape measures which have been unfolded for the effects of detector resolution and acceptance and for initial-state radiation by the three experiments. We do not include the ERT-E0 Monte Carlo in this study because this Monte Carlo cannot be expected

to describe data at very different c.m. energies using the same parameter set.

Figures 4 (a), (b) and (c) show the OPAL measurements of the Thrust, Sphericity and Aplanarity distributions in comparison to those of TASSO and MARK2. The peaking of the Sphericity and Aplanarity distributions toward low values for the 91 GeV data, relative to the lower energy data, and the corresponding peaking of the Thrust distribution toward high values, can be attributed to two sources: (1) jet narrowing associated with the larger c.m. energy, which is a kinematical effect related to the lessened importance of fragmentation as a mechanism to populate the tails of the distributions as the c.m. energy increases, and (2) QCD scaling violations associated with a smaller rate for acolinear gluon radiation at higher c.m. energies. Monte Carlo studies employing Jetset and Herwig demonstrate that over 50 per cent of the difference in the shape of the Thrust and Sphericity distributions between 29 and 91 GeV can be attributed to scaling violations, for certain regions, while the difference in the shape of the Aplanarity distribution between the different energies is almost entirely related to jet narrowing. For example, the Thrust distribution  $1/N_0 (dN/dT)$  decreases in value by about 44 per cent between the MARK2 and OPAL measurements for the region of Thrust between 0.72 and 0.88. By using Jetset to unfold these distributions for fragmentation, using the matrix technique of equation 12, we deduce that a decrease of about 25 per cent is expected in this region because of the change in the parton state by itself; the corresponding number we derive from Herwig is 22 per cent. Thus about half of the difference between the MARK2 and OPAL measurements for the Thrust region below about 0.7 can be attributed to a QCD scaling violation according to these studies. An analogous study of the Sphericity distribution above values of 0.3 shows that more than 70 per cent of the difference between the MARK2 and OPAL measurements in this region can be attributed to a scaling violation. The unfolding of the distributions for fragmentation is to the level of parton virtuality which exists at the end of the perturbative shower in Jetset or in Herwig.

We now discuss the descriptions of the data at the three c.m. energies by the optimized Monte Carlo programs. Jetset72 provides a good description of the measurements for the three c.m. energies, as observed from figure 4. This is not particularly surprising given that our optimized parameter set for Jetset is not very different from that of TASSO. The slightly low prediction of Jetset for the tail of Aplanarity at 91 GeV is not present for the lower c.m. energies. The corresponding study for Herwig34 is shown in figure 5. Herwig also provides a good overall description of the measurements for the three c.m. energies except that its predictions are too peaked toward the high Thrust region at 29 and 35 GeV and there is some discrepancy with the 29 GeV data for the lowest bin of Sphericity and Aplanarity. For Aplanarity, the Herwig prediction at 91 GeV agrees well with measurement: this is less the case at 29 or 35 GeV for which the Herwig predictions lie above the data in the tail. This suggests a similarity in the energy scaling behavior of Jetset and Herwig in that the Aplanarity distribution predicted by both Monte Carlos becomes softer, in comparison to data, as the c.m. energy increases. Ariadne also provides a good description of the measurements for the three c.m. energies, as presented in figure 6, except for a difference between the model predictions and data for the highest bin of Thrust and for the lowest bin of Sphericity and of Aplanarity at 29 GeV. This is analogous to the situation we observe for Herwig for these same bins. The Aplanarity distribution of Ariadne softens slightly too much relative to data with increased c.m. energy as we observe also for Jetset and for Herwig.

The  $\chi^2$  values between the measurements and QCD models are given in table 15 for the three c.m. energies. From this table, it is seen that the  $\chi^2$  values between the MARK2 data and Jetset are considerably smaller than they are between the MARK2 data and Herwig or the MARK2 data and Ariadne. By far the largest contributors to the  $\chi^2$  values of Herwig and Ariadne are the one or two lowest (for Sphericity and Aplanarity) or highest (for Thrust) histogram bins, however. We also include in table 15 the  $\chi^2$  values between the MARK2 data and Monte Carlo predictions with the last two bins of Thrust, the first two bins of Sphericity and the first bin of Aplanarity excluded. These latter  $\chi^2$  values possibly allow a more meaningful assessment of the descriptions of the 29 GeV data by Herwig and Ariadne.

The data in figures 4, 5 and 6 and in table 15 demonstrate that, globally, all three QCD parton shower models provide quite satisfactory descriptions of the measurements for the three c.m. energies.

## 10 Summary

We have presented experimental measurements of distributions which characterize global event structure in the hadronic decays of the  $Z^0$ . These measurements are based on a sample of 29,197 multi-hadronic  $Z^0$  decay events which have been collected with the OPAL detector at LEP. We have unfolded most of these distributions for the effects of detector resolution and acceptance and for initial-state photon radiation. The values of the principal parameters of Jetset72, Herwig34, Ariadne31 and a second order ERT-based matrix element Monte Carlo with a modified perturbation scale (ERT-E0) have been adjusted to describe the unfolded  $T_{major}$  and  $(H_2/H_0)$  distributions.

Our optimized parameter values for Jetset do not differ significantly from those found by the TASSO collaboration at a c.m. energy of 35 GeV [27] but they are quite different from the default values and from those of the MARK2 collaboration [31]. For the Herwig, Ariadne and ERT-E0 models, our optimized parameter sets are quite different from those provided by the authors. After adjusting the parameter values to best describe the  $T_{major}$  and  $(H_2/H_0)$  distributions, we find that Jetset, Herwig and Ariadne, all of which are based on a parton shower, provide good descriptions of the other unfolded event shape distributions. Since the tuning procedure does not constrain all degrees-of-freedom which describe multi-hadronic event structure, this agreement of the QCD models demonstrates their general consistency for describing the 91 GeV data. The ERT-E0 model provides a reasonable description of some regions of the distributions which are dominated by three jet production, such as the tail of the Thrust distribution, but – as expected – it does not describe the two jet region well. The ERT-E0 model also displays discrepancy with the data for distributions based on momentum out of the event plane, such as  $T_{minor}$  and Aplanarity.

The unfolded event shape distributions are based on measurements with the electromagnetic calorimeter. We include detector simulation and initial-state radiation with the models' predictions, using our optimized parameter sets, and compare to charged track based distributions. We observe the same trends between Monte Carlo description and the charged track measurements at this detector level, using  $T_{major}$  and  $(H_2/H_0)$  as examples, as we observe

between Monte Carlo description and the calorimeter measurements at the unfolded level. The charged track based predictions of Herwig and Jetset for  $\langle n_{ch.} \rangle$  and  $\ln(1/x_p)$  are also in agreement with our observations, further establishing the consistency of the QCD model description of the 91 GeV data. We obtain an unfolded value for the mean charged multiplicity of  $\langle n_{ch.} \rangle = 21.28 \pm 0.04 \pm 0.84$ .

Herwig, Jetset and Ariadne with the adjusted parameter sets provide, in addition, a good description of multi-hadronic event structure as observed at about one third our c.m. energy value by the TASSO and MARK2 collaborations. This demonstrates the consistency of the QCD models for describing the detailed features of global event structure in  $e^+e^-$  multi-hadronic annihilations over a very large energy range.

## 11 Acknowledgements

It is a pleasure to thank the LEP Division for the efficient operation of the machine and their continuing close cooperation with our experimental group. In addition to the support staff at our own institutions we are pleased to acknowledge the following: The Bundesministerium für Forschung und Technologie, FRG, The Department of Energy, USA, The Institut de Recherche Fondamentale du Commissariat à l'Énergie Atomique, The Israeli Ministry of Science, The Minerva Gesellschaft, The National Science Foundation, USA, The Natural Sciences and Engineering Research Council, Canada, The Japanese Ministry of Education, Science and Culture (the Monbusho) and a grant under the Monbusho International Science Research Program, The Science and Engineering Research Council, UK and The A. P. Sloan Foundation.

## References

- [1] OPAL Technical proposal (1983) and CERN/LEPC/83-4;  
OPAL Collaboration, K. Ahmet *et al.*, The OPAL Detector at LEP, to be submitted to Nucl. Instr. and Meth.
- [2] OPAL Collaboration, M.Z. Akrawy *et al.*, Phys. Lett. B235 (1990) 379.
- [3] OPAL Collaboration, M.Z. Akrawy *et al.*, Phys. Lett. B231 (1989) 530.
- [4] S. Brandt *et al.*, Phys.Lett. **12** (1964) 57;  
E. Fahri, Phys.Rev.Lett. **39** (1977) 1587.
- [5] J.D. Bjorken and S.J. Brodsky, Phys.Rev. **D1** (1970) 1416.
- [6] R.K. Ellis, D.A. Ross, A.E. Terrano, Nucl.Phys. **B178** (1981) 421.
- [7] G. Parisi, Phys. Lett. **74B** (1978) 65;  
J.F. Donoghue, F.E. Low and S.Y. Pi, Phys.Rev. **D20** (1979) 2759.
- [8] G.C. Fox and S. Wolfram, Nucl.Phys. **B149** (1979) 413.
- [9] T. Sjöstrand, Comp.Phys.Comm. **39** (1986) 347;  
T. Sjöstrand and M. Bengtsson, Comp.Phys.Comm. **43** (1987) 367.
- [10] G. Marchesini and B.R. Webber, Nucl.Phys. **B310** (1988) 461.
- [11] A. Ali, Phys.Lett **110B** (1982) 67;  
A. Ali and F. Barreiro, Nucl.Phys. **B118** (1982) 155;  
A. Ali and F. Barreiro, Nucl.Phys. **B236** (1984) 269.
- [12] N. Magnussen, Wuppertal Ph.D. Thesis, WUB-DI 88-4 (1988) and DESY internal report F22-89-01 (1989); we received this program from N. Magnussen in February 1989.
- [13] U. Petterson, LU TP 88-5 (1988);  
L. Lönnblad and U. Petterson, LU TP 88-15 (1988);  
L. Lönnblad, LU TP 89-10 (1988).
- [14] For reviews, see L.A. Gribov, E.M. Levin and M.G. Ryskin, Phys.Rep. **100** (1983) 1;  
A. Bassetto, M. Ciafaloni and G. Marchesini, Phys.Rep. **100** (1983) 201;  
B.R. Webber, Ann.Rev.Nucl.Part.Sci. **36** (1986) 253.
- [15] B. Andersson *et al.*, Phys.Rep. **97** (1983) 31.
- [16] F.A. Berends, R. Kleiss and S. Jadach, Nucl.Phys. **B202** (1982) 63; Comp.Phys.Comm. **29** (1983) 185.
- [17] I.G. Knowles, Nucl.Phys. **B310** (1988) 571.
- [18] G.C. Fox and S. Wolfram, Nucl. Phys. **B168** (1980) 285.

- [19] Ya.I. Azimov *et al.*, Phys. Lett. **B165** (1985) 147;  
G. Gustafson, Phys. Lett. **B175** (1986) 453;  
G. Gustafson and U. Pettersson, Nucl. Phys. **B306** (1988) 746.
- [20] S. Bethke, Z. Phys. **C43** (1989) 331;  
AMY Collaboration, Phys. Rev. Lett. **62** (1989) 1713;  
OPAL Collaboration, M.Z. Akrawy *et al.*, Phys. Lett. **B235** (1990) 389.
- [21] Z. Kunszt and P. Nason, Z Physics at LEP 1, Vol. 1, CERN 89-08, eds. G. Altarelli, R. Kleiss and C. Verzegnassi, Geneva 1989.
- [22] J. Allison *et al.*, Comp. Phys. Comm. **47** (1987) 55.
- [23] R. Brun *et al.*, GEANT3 User's Guide, CERN DD/EE/84-1 (1989).
- [24] V. Blobel, DESY report 84-118 (1984).
- [25] OPAL Collaboration, M.Z. Akrawy *et al.*, Phys. Lett. **B236** (1990) 364.
- [26] TPC Collaboration, H. Aihara *et al.*, Z. Phys. **C28** (1985) 31;  
J.W. Gary, U.of California Ph.D Thesis, LBL-20638 (1985).
- [27] TASSO Collaboration, W. Braunschweig *et al.*, Z. Phys. **C41** (1988) 375.
- [28] ALEPH collaboration, D. Decamp *et al.*, Phys. Lett. **234B** (1990) 209.
- [29] DELPHI Collaboration, P. Aarnio *et al.*, CERN-EP/90-19, February 1990.
- [30] MARK2 Collaboration, G.S. Abrams *et al.*, Phys.Rev.Lett. **64** (1990) 1334.
- [31] MARK2 Collaboration, A. Petersen *et al.*, Phys. Rev. **D37** (1988) 1.



## Figure Captions

Figure 1: Herwig events with detector simulation and initial-state radiation which have been unfolded using Jetset (points with error bars) compared to Herwig (solid curve) and Jetset (dashed curve) without detector simulation or initial-state radiation.

Figure 2: The unfolded event shape distributions at 91 GeV. The errors on the data points include the full statistical and systematic errors. The predictions of the QCD models with their optimized parameter values are also shown. The statistical errors on the model predictions are typically three to four times smaller than the errors shown for the data. The small inset above each distribution shows the correction constants used for unfolding; the inset below each distribution shows the difference between the model predictions and data in units of standard deviation, calculated using the full errors. The distributions are normalized to the number of events  $N_0$  in the samples.

Figure 3: Event shape distributions based on charged tracks, compared to the predictions of Jetset and Herwig with their optimized parameter values. The data are not unfolded; the Monte Carlo predictions include detector simulation and initial-state radiation. There are about 4,000 events in the Monte Carlo samples. The distributions are normalized to the number of events  $N_0$  in the samples.

Figure 4: Unfolded measurements of the Thrust, Sphericity and Aplanarity distributions at 91, 35 and 29 GeV, compared to the predictions of Jetset72 with its optimized parameter values. The 29 GeV curve for Thrust and Sphericity is shown on a reduced scale to simplify the figure.

Figure 5: Unfolded measurements of the Thrust, Sphericity and Aplanarity distributions at 91, 35 and 29 GeV, compared to the predictions of Herwig34 with its optimized parameter values.

Figure 6: Unfolded measurements of the Thrust, Sphericity and Aplanarity distributions at 91, 35 and 29 GeV, compared to the predictions of Ariadne31 with its optimized parameter values.

Table 1: The main parameters of Jetset version 7.2 which control the momentum distribution of hadrons. The values of  $\Lambda_{QCD}$ ,  $Q_0$ ,  $\sigma_q$  and  $a$  are optimized through comparison with our data. The error assigned to a parameter is an estimate of the one standard deviation value, which describes the variation which is permitted to the parameter while remaining in agreement with our global event shape measurements (including  $\langle n_{ch.} \rangle$ ) when the other parameters remain fixed.

Parameter	Monte Carlo name	Default Value	Optimized Value
$\Lambda_{QCD}$	PARJ(81)	0.40 GeV	$0.29^{+0.02}_{-0.01}$ GeV
$Q_0$	PARJ(82)	1.0 GeV	$1.0^{+0.8}_{-0.3}$ GeV
$\sigma_q$	PARJ(21)	0.35 GeV	$0.37^{+0.03}_{-0.05}$ GeV
$a$	PARJ(41)	0.50	$0.18^{+0.12}_{-0.05}$
$b$	PARJ(42)	0.90 GeV <sup>-2</sup>	0.34 GeV <sup>-2</sup>

Table 2: The main parameters of Herwig version 3.4 which control the momentum distribution of hadrons. The values of the three parameters  $\Lambda_{QCD}$ ,  $m_g$  and  $M_{max}$  are optimized through comparison with our data. The errors assigned to the parameter values have the same meaning as for table 1.

Parameter	Monte Carlo name	Default Value	Optimized Value
$\Lambda_{QCD}$	QC DLAM	0.20 GeV	$0.110 \pm 0.007$ GeV
$m_g$	RMASS(13)	0.65 GeV	$0.65^{+0.08}_{-0.01}$ GeV
$M_{max}$	CLMAX	5.0 GeV	$3.0^{+0.4}_{-0.8}$ GeV

Table 3: The main parameters of Ariadne version 3.1 which control the momentum distribution of hadrons. The values of  $\Lambda_{QCD}$ ,  $P_T^{min}$  and  $\sigma_q$  are optimized through comparison with our data. The errors assigned to the parameter values have the same meaning as for table 1.

Parameter	Monte Carlo name	Default Value	Optimized Value
$\Lambda_{QCD}$	VAR(1)	0.25 GeV	$0.20 \pm 0.02$ GeV
$P_T^{min}$	VAR(3)	0.50 GeV/c	$1.0_{-0.4}^{+0.2}$ GeV/c
$\sigma_q$	PARJ(21)	0.35 GeV	$0.37 \pm 0.04$ GeV
$a$	PARJ(41)	0.50	0.18
$b$	PARJ(42)	0.90 GeV <sup>-2</sup>	0.34 GeV <sup>-2</sup>

Table 4: The main parameters of the ERF-E0 matrix element Monte Carlo which control the momentum distribution of hadrons. The values of  $\sigma_q$ ,  $a$  and  $b$  are optimized through comparison with our data.

Parameter	Monte Carlo name	Default Value	Optimized Value
$\sigma_q$	PAR(12)	0.425 GeV	0.520 GeV
$a$	PAR(31)	1.00	1.20
$b$	PAR(32)	0.60 GeV <sup>-2</sup>	0.60 GeV <sup>-2</sup>
$y_{min}$	PARE(8)	0.015	0.010
$\Lambda_{\overline{MS}}$	PARE(2)	0.090 GeV	—
$k$ , optimized scale factor	XAP	0.005	—

Table 5: The unfolded Thrust distribution at 91 GeV. The first error is statistical and includes the statistical uncertainty for the correction factor, the second is systematic.

Bin nr.	Thrust Range	$1/N_0 ( dN/dT )$		
1	0.50-0.62	0.0014	$\pm 0.0008$	$\pm 0.012$
2	0.62-0.72	0.142	$\pm 0.016$	$\pm 0.028$
3	0.72-0.76	0.389	$\pm 0.034$	$\pm 0.085$
4	0.76-0.80	0.623	$\pm 0.051$	$\pm 0.104$
5	0.80-0.82	0.842	$\pm 0.075$	$\pm 0.103$
6	0.82-0.84	1.182	$\pm 0.092$	$\pm 0.092$
7	0.84-0.86	1.405	$\pm 0.092$	$\pm 0.071$
8	0.86-0.88	1.88	$\pm 0.11$	$\pm 0.04$
9	0.88-0.90	2.64	$\pm 0.14$	$\pm 0.01$
10	0.90-0.92	3.60	$\pm 0.16$	$\pm 0.01$
11	0.92-0.94	5.49	$\pm 0.19$	$\pm 0.14$
12	0.94-0.97	10.60	$\pm 0.22$	$\pm 0.26$
13	0.97-1.00	9.58	$\pm 0.18$	$\pm 0.44$
mean	0.50-1.00	0.9309	$\pm 0.0007$	$\pm 0.0041$

Table 6: The unfolded  $T_{major}$  distribution at 91 GeV.

Bin nr.	$T_{major}$ Range	$1/N_0 ( dN/dT_{major} )$		
1	0.00-0.06	---		
2	0.06-0.12	5.84	$\pm 0.11$	$\pm 0.07$
3	0.12-0.16	4.39	$\pm 0.11$	$\pm 0.07$
4	0.16-0.20	2.902	$\pm 0.091$	$\pm 0.07$
5	0.20-0.24	2.188	$\pm 0.083$	$\pm 0.05$
6	0.24-0.28	1.690	$\pm 0.074$	$\pm 0.032$
7	0.28-0.32	1.227	$\pm 0.061$	$\pm 0.009$
8	0.32-0.40	0.770	$\pm 0.035$	$\pm 0.030$
9	0.40-0.48	0.433	$\pm 0.026$	$\pm 0.076$
10	0.48-0.64	0.147	$\pm 0.010$	$\pm 0.043$
11	0.64-0.80	0.00184	$\pm 0.00075$	$\pm 0.002$
mean	0.06-0.80	0.1856	$\pm 0.0013$	$\pm 0.0056$

Table 7: The unfolded  $T_{minor}$  distribution at 91 GeV.

Bin nr.	$T_{minor}$ Range	$1/N_0 (dN/dT_{minor})$		
1	0.00-0.04	—		
2	0.04-0.06	6.87	$\pm 0.18$	$\pm 1.70$
3	0.06-0.08	11.88	$\pm 0.28$	$\pm 0.50$
4	0.08-0.10	10.80	$\pm 0.28$	$\pm 0.86$
5	0.10-0.12	7.11	$\pm 0.22$	$\pm 0.50$
6	0.12-0.14	4.46	$\pm 0.17$	$\pm 0.01$
7	0.14-0.16	2.78	$\pm 0.13$	$\pm 0.02$
8	0.16-0.18	1.65	$\pm 0.10$	$\pm 0.02$
9	0.18-0.20	1.043	$\pm 0.081$	$\pm 0.018$
10	0.20-0.24	0.586	$\pm 0.048$	$\pm 0.020$
11	0.24-0.28	0.248	$\pm 0.033$	$\pm 0.023$
12	0.28-0.36	0.070	$\pm 0.011$	$\pm 0.009$
13	0.36-0.44	0.0121	$\pm 0.0055$	$\pm 0.009$
14	0.44-0.52	0.0017	$\pm 0.0012$	$\pm 0.002$
mean	0.04-0.52	0.1009	$\pm 0.0006$	$\pm 0.0032$

Table 8: The unfolded Oblateness distribution at 91 GeV.

Bin nr.	Oblateness Range	$1/N_0 (dN/dO)$		
1	0.00-0.03	10.24	$\pm 0.22$	$\pm 0.28$
2	0.03-0.06	8.58	$\pm 0.18$	$\pm 0.12$
3	0.06-0.08	4.66	$\pm 0.16$	$\pm 0.007$
4	0.08-0.10	3.23	$\pm 0.13$	$\pm 0.24$
5	0.10-0.12	2.50	$\pm 0.12$	$\pm 0.18$
6	0.12-0.14	2.08	$\pm 0.11$	$\pm 0.16$
7	0.14-0.16	1.70	$\pm 0.11$	$\pm 0.06$
8	0.16-0.20	1.381	$\pm 0.064$	$\pm 0.01$
9	0.20-0.24	0.859	$\pm 0.050$	$\pm 0.100$
10	0.24-0.28	0.569	$\pm 0.037$	$\pm 0.113$
11	0.28-0.36	0.357	$\pm 0.023$	$\pm 0.116$
12	0.36-0.48	0.112	$\pm 0.010$	$\pm 0.026$
mean	0.00-0.48	0.0825	$\pm 0.0009$	$\pm 0.0057$



Table 9: The unfolded Sphericity distribution at 91 GeV.

Bin nr.	Sphericity Range	$1/N_0 ( dN/dS )$		
1	0.00-0.02	17.90	$\pm 0.30$	$\pm 0.29$
2	0.02-0.04	10.07	$\pm 0.26$	$\pm 0.12$
3	0.04-0.06	5.35	$\pm 0.18$	$\pm 0.08$
4	0.06-0.08	3.27	$\pm 0.15$	$\pm 0.05$
5	0.08-0.10	2.40	$\pm 0.13$	$\pm 0.00$
6	0.10-0.12	1.70	$\pm 0.11$	$\pm 0.03$
7	0.12-0.14	1.304	$\pm 0.089$	$\pm 0.028$
8	0.14-0.16	1.080	$\pm 0.092$	$\pm 0.028$
9	0.16-0.18	0.809	$\pm 0.071$	$\pm 0.028$
10	0.18-0.20	0.737	$\pm 0.073$	$\pm 0.028$
11	0.20-0.24	0.585	$\pm 0.049$	$\pm 0.028$
12	0.24-0.28	0.456	$\pm 0.044$	$\pm 0.028$
13	0.28-0.36	0.301	$\pm 0.022$	$\pm 0.028$
14	0.36-0.44	0.177	$\pm 0.017$	$\pm 0.026$
15	0.44-0.60	0.1093	$\pm 0.0098$	$\pm 0.023$
16	0.60-0.80	0.0326	$\pm 0.0055$	$\pm 0.015$
17	0.80-1.00	0.00141	$\pm 0.00065$	$\pm 0.0010$
mean	0.00-1.00	0.0772	$\pm 0.0014$	$\pm 0.0060$

Table 10: The unfolded Aplanarity distribution at 91 GeV.

Bin nr.	Aplanarity Range	$1/N_0$ ( dN/dA )		
1	0.000-0.006	72.1	$\pm 1.1$	$\pm 5.48$
2	0.006-0.012	45.7	$\pm 1.1$	$\pm 3.51$
3	0.012-0.016	21.26	$\pm 0.89$	$\pm 0.83$
4	0.016-0.020	12.95	$\pm 0.68$	$\pm 0.50$
5	0.020-0.024	8.27	$\pm 0.51$	$\pm 0.08$
6	0.024-0.028	6.30	$\pm 0.50$	$\pm 0.07$
7	0.028-0.032	4.36	$\pm 0.42$	$\pm 0.07$
8	0.032-0.040	2.73	$\pm 0.20$	$\pm 0.06$
9	0.040-0.048	1.84	$\pm 0.17$	$\pm 0.05$
10	0.048-0.056	1.27	$\pm 0.16$	$\pm 0.04$
11	0.056-0.072	0.714	$\pm 0.077$	$\pm 0.02$
12	0.072-0.088	0.425	$\pm 0.061$	$\pm 0.006$
13	0.088-0.104	0.244	$\pm 0.041$	$\pm 0.006$
14	0.104-0.136	0.115	$\pm 0.021$	$\pm 0.016$
15	0.136-0.168	0.058	$\pm 0.022$	$\pm 0.016$
16	0.168-0.200	0.021	$\pm 0.010$	$\pm 0.001$
17	0.200-0.230	0.0134	$\pm 0.0071$	$\pm 0.029$
mean	0.000-0.230	0.01241	$\pm 0.00021$	$\pm 0.00080$

Table 11: The unfolded  $D$  Variable distribution at 91 GeV.

Bin nr.	$D$ Variable Range	$1/N_0 ( dN/dD )$		
1	0.000-0.025	18.58	$\pm 0.28$	$\pm 0.40$
2	0.025-0.050	6.95	$\pm 0.19$	$\pm 0.03$
3	0.050-0.075	3.86	$\pm 0.15$	$\pm 0.01$
4	0.075-0.100	2.41	$\pm 0.11$	$\pm 0.003$
5	0.100-0.125	1.704	$\pm 0.093$	$\pm 0.007$
6	0.125-0.150	1.288	$\pm 0.085$	$\pm 0.015$
7	0.150-0.175	1.038	$\pm 0.083$	$\pm 0.022$
8	0.175-0.200	0.855	$\pm 0.071$	$\pm 0.027$
9	0.200-0.250	0.549	$\pm 0.038$	$\pm 0.033$
10	0.250-0.300	0.379	$\pm 0.033$	$\pm 0.037$
11	0.300-0.400	0.211	$\pm 0.019$	$\pm 0.038$
12	0.400-0.500	0.095	$\pm 0.014$	$\pm 0.029$
13	0.500-0.600	0.0422	$\pm 0.0072$	$\pm 0.016$
14	0.600-0.700	0.0201	$\pm 0.0059$	$\pm 0.0007$
15	0.700-0.800	0.0127	$\pm 0.0053$	$\pm 0.0055$
16	0.800-1.000	0.0029	$\pm 0.0013$	$\pm 0.0037$
mean	0.000-1.000	0.0691	$\pm 0.0012$	$\pm 0.0054$

Table 12: The unfolded ( $H_2/H_0$ ) distribution at 91 GeV.

Bin nr.	( $H_2/H_0$ ) Range	$1/N_0 ( dN/d(H_2/H_0) )$		
1	0.000-0.150	0.0308	$\pm 0.0057$	$\pm 0.0175$
2	0.150-0.300	0.260	$\pm 0.016$	$\pm 0.049$
3	0.300-0.450	0.475	$\pm 0.021$	$\pm 0.053$
4	0.450-0.550	0.634	$\pm 0.028$	$\pm 0.021$
5	0.550-0.600	0.894	$\pm 0.052$	$\pm 0.058$
6	0.600-0.650	1.012	$\pm 0.051$	$\pm 0.065$
7	0.650-0.700	1.279	$\pm 0.057$	$\pm 0.056$
8	0.700-0.750	1.625	$\pm 0.065$	$\pm 0.030$
9	0.750-0.800	2.154	$\pm 0.073$	$\pm 0.006$
10	0.800-0.850	2.960	$\pm 0.089$	$\pm 0.037$
11	0.850-0.925	3.691	$\pm 0.079$	$\pm 0.035$
12	0.925-1.000	—		
mean	0.000-0.925	0.7130	$\pm 0.0023$	$\pm 0.0104$

Table 13: The  $\chi^2$  values between the unfolded event shape distributions and the optimized Monte Carlo predictions. There are 50,000 events in the Monte Carlo samples.

Distribution	Nr.bins	Jetset72	Herwig34	Ariadnc31	ERT-E0
Thrust $T$	13	5.0	14.8	8.6	21.9
$T_{minor}$	13	12.1	15.1	14.1	118.3
$T_{major}$	10	7.7	8.4	7.1	17.0
Oblateness $O$	12	6.0	13.5	9.4	30.8
Sphericity $S$	17	8.5	14.2	6.1	13.5
Aplanarity $A$	17	10.1	7.3	10.4	84.2
The $D$ variable	16	5.0	21.6	18.2	24.7
( $H_2/H_0$ )	11	4.0	6.2	5.0	23.7
Totals	109	58.4	101.1	78.9	334.1

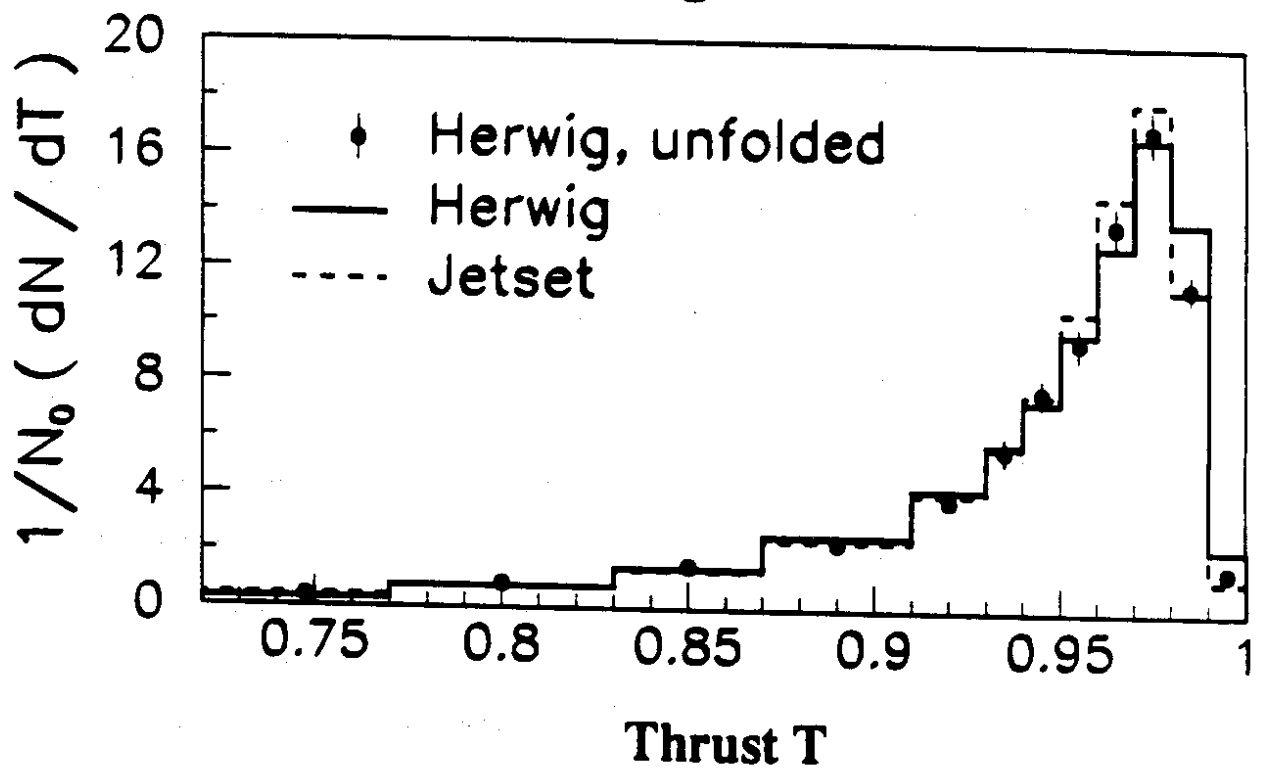
Table 14: The  $\chi^2$  values between the data and optimized Monte Carlo predictions for charged track based distributions. The data are not unfolded; the Monte Carlo predictions include detector simulation and initial-state radiation. There are about 4,000 events in the Monte Carlo samples.

Distribution	Nr.bins	Jetset72	Herwig34
$n_{ch.}$	39	51.3	48.9
$T_{major}$	32	28.7	31.0
$(H_2/H_0)$	27	20.1	33.1
$\ln(1/x_p)$	29	45.9	49.8
Totals	127	146.0	162.8

Table 15: The  $\chi^2$  values between the Monte Carlos optimized at 91 GeV and the unfolded OPAL, TASSO and MARK2 measurements, for the Thrust, Sphericity and Aplanarity distributions. There are 50,000 events in the Monte Carlo samples.

	OPAL (91 GeV)	TASSO (35 GeV)	MARK2 (29GeV)
Thrust			
Jetset72	5.0 (13 bins)	11.5 (14 bins)	16.8 (22 bins) 13.7 (20 bins)
Herwig34	14.8 (13 bins)	70.2 (14 bins)	141.4 (22 bins) 86.2 (20 bins)
Ariadne31	8.6 (13 bins)	5.6 (14 bins)	74.7 (22 bins) 33.4 (20 bins)
Sphericity			
Jetset72	8.5 (17 bins)	13.9 (18 bins)	30.1 (40 bins) 28.1 (38 bins)
Herwig34	14.2 (17 bins)	39.9 (18 bins)	160.2 (40 bins) 69.9 (38 bins)
Ariadne31	6.1 (17 bins)	10.0 (18 bins)	127.4 (40 bins) 34.2 (38 bins)
Aplanarity			
Jetset72	10.1 (17 bins)	17.0 (11 bins)	31.0 (24 bins) 30.6 (23 bins)
Herwig34	7.3 (17 bins)	29.0 (11 bins)	122.1 (24 bins) 87.0 (23 bins)
Ariadne31	10.4 (17 bins)	12.0 (11 bins)	62.1 (24 bins) 32.8 (23 bins)

Figure 1



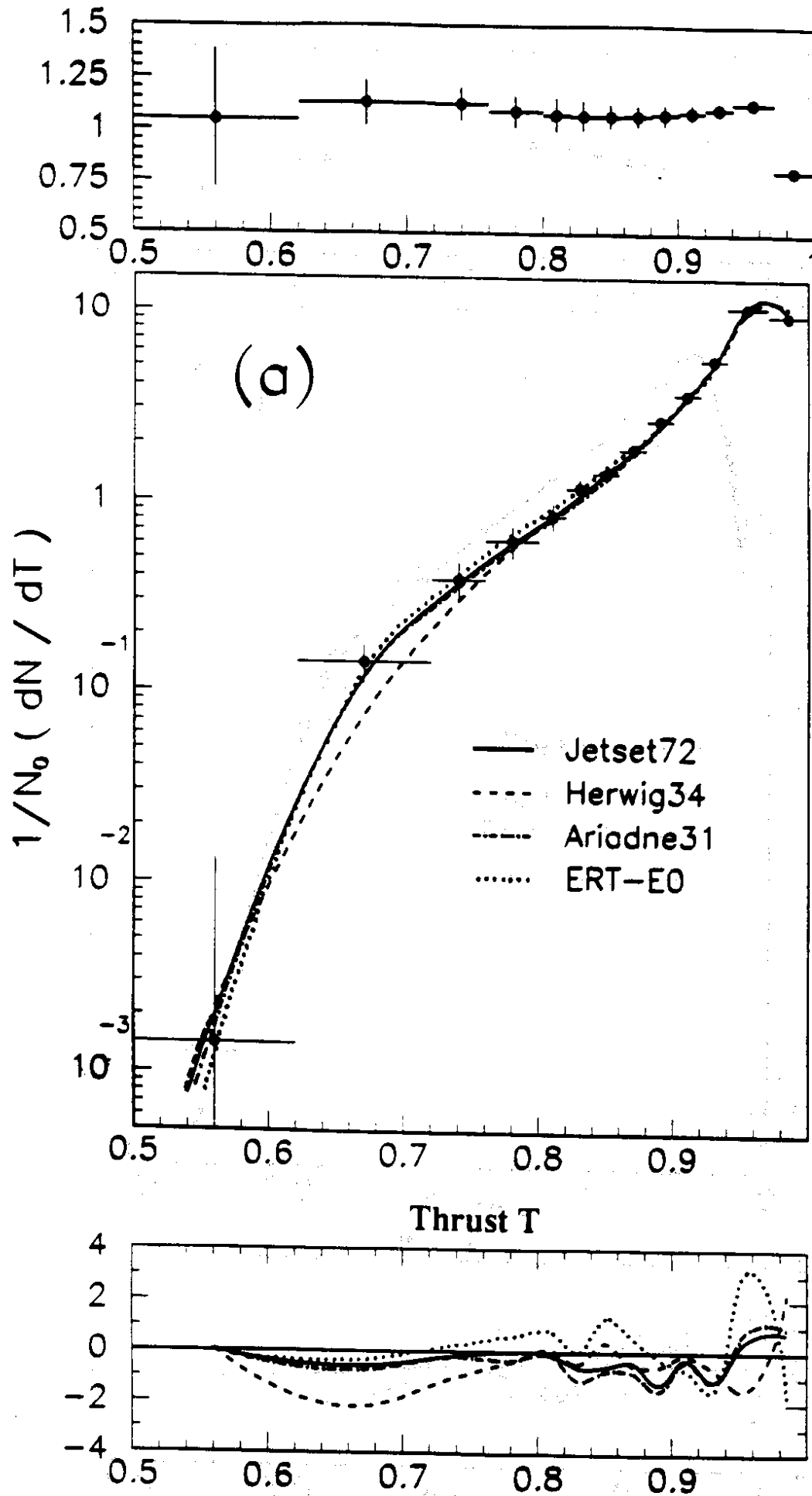


Figure 2



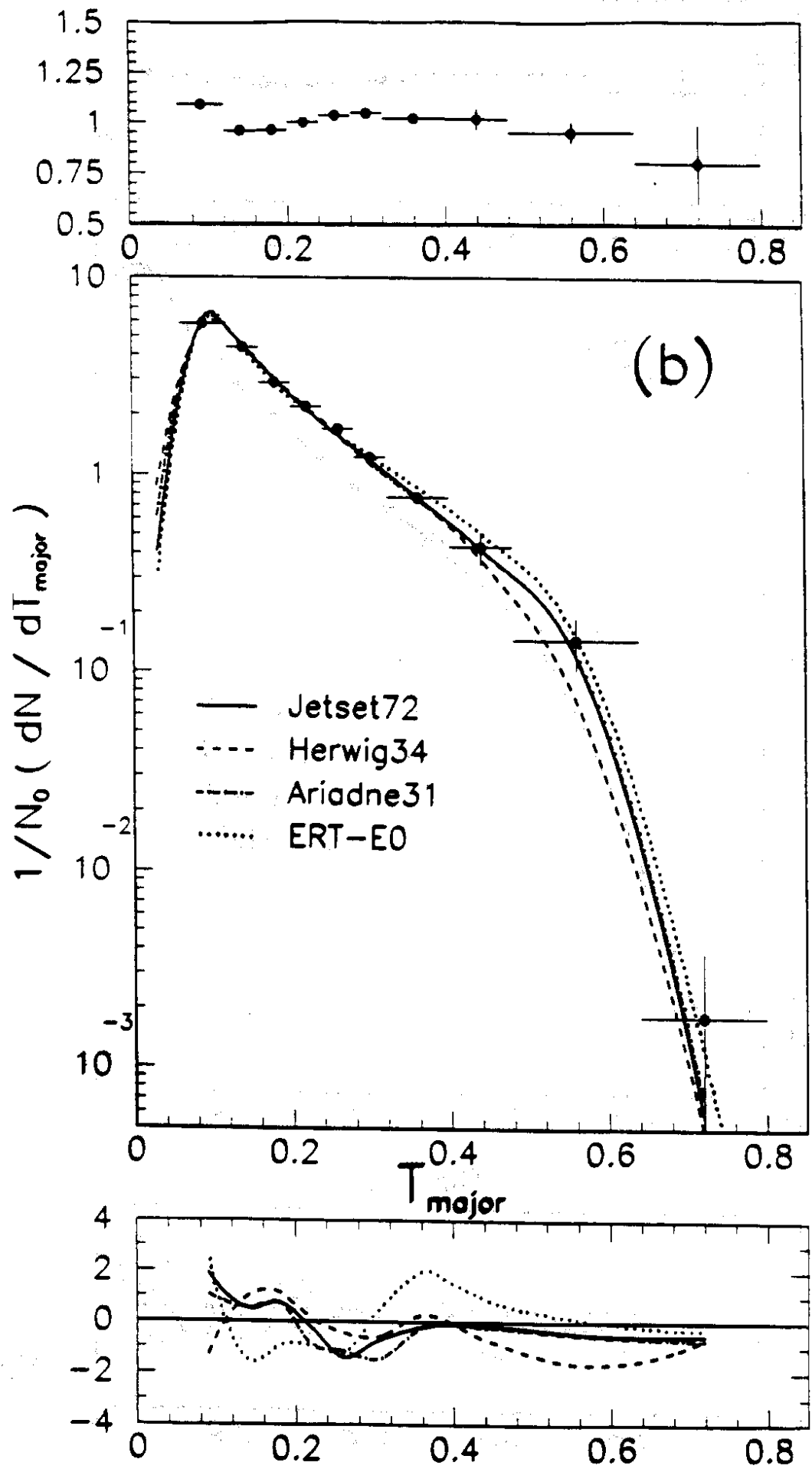


Figure 2

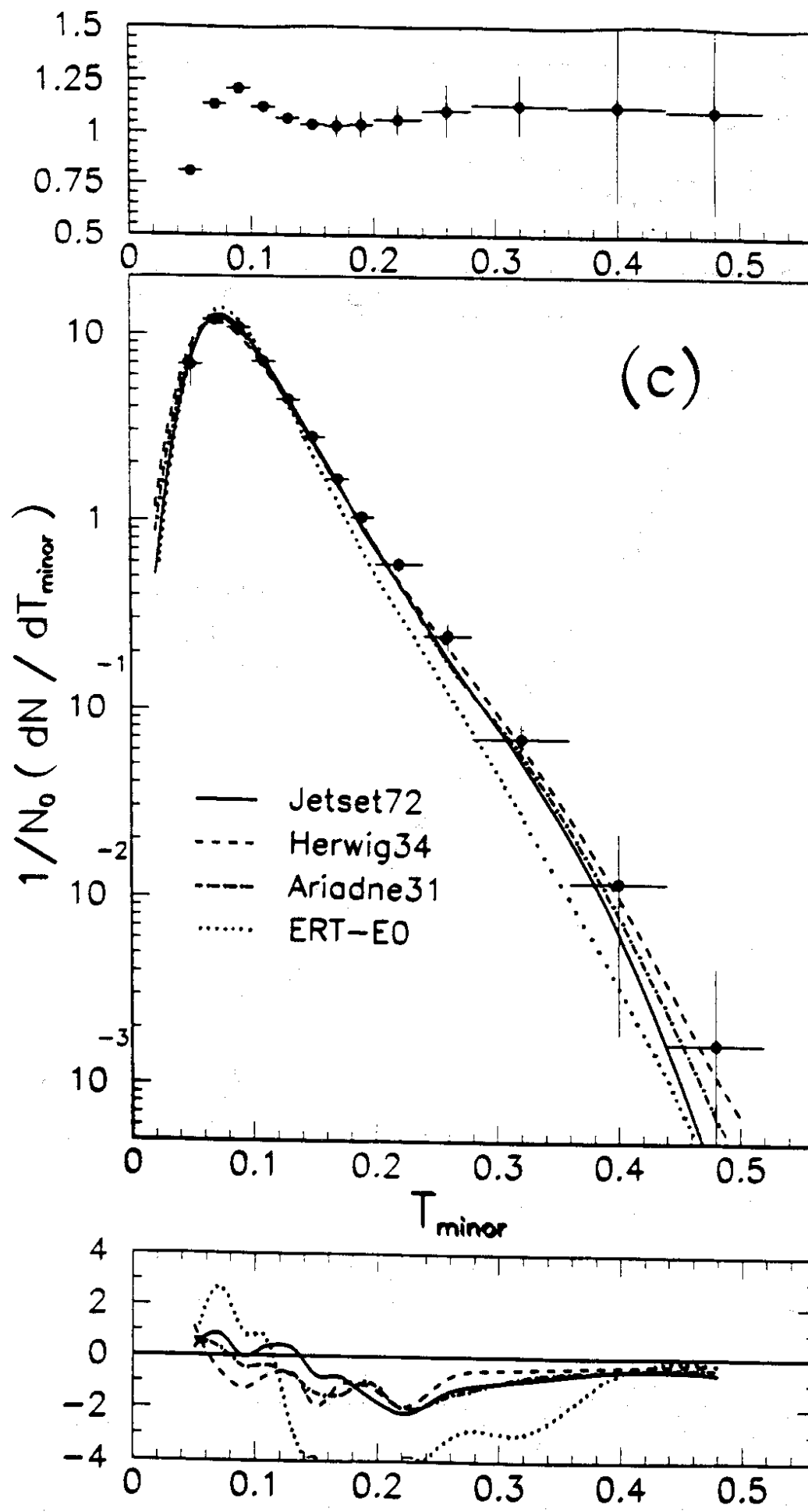


Figure 2

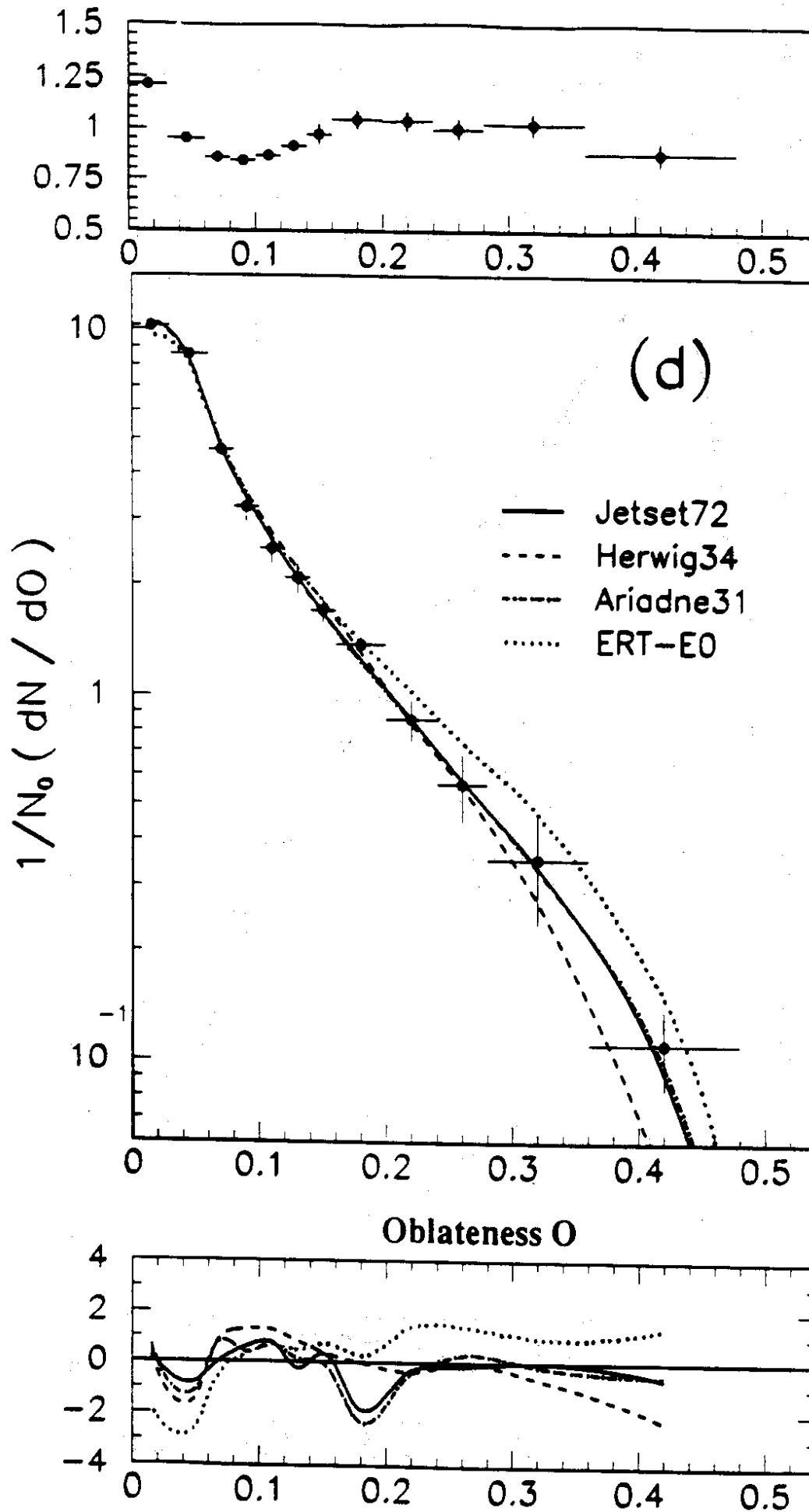


Figure 2

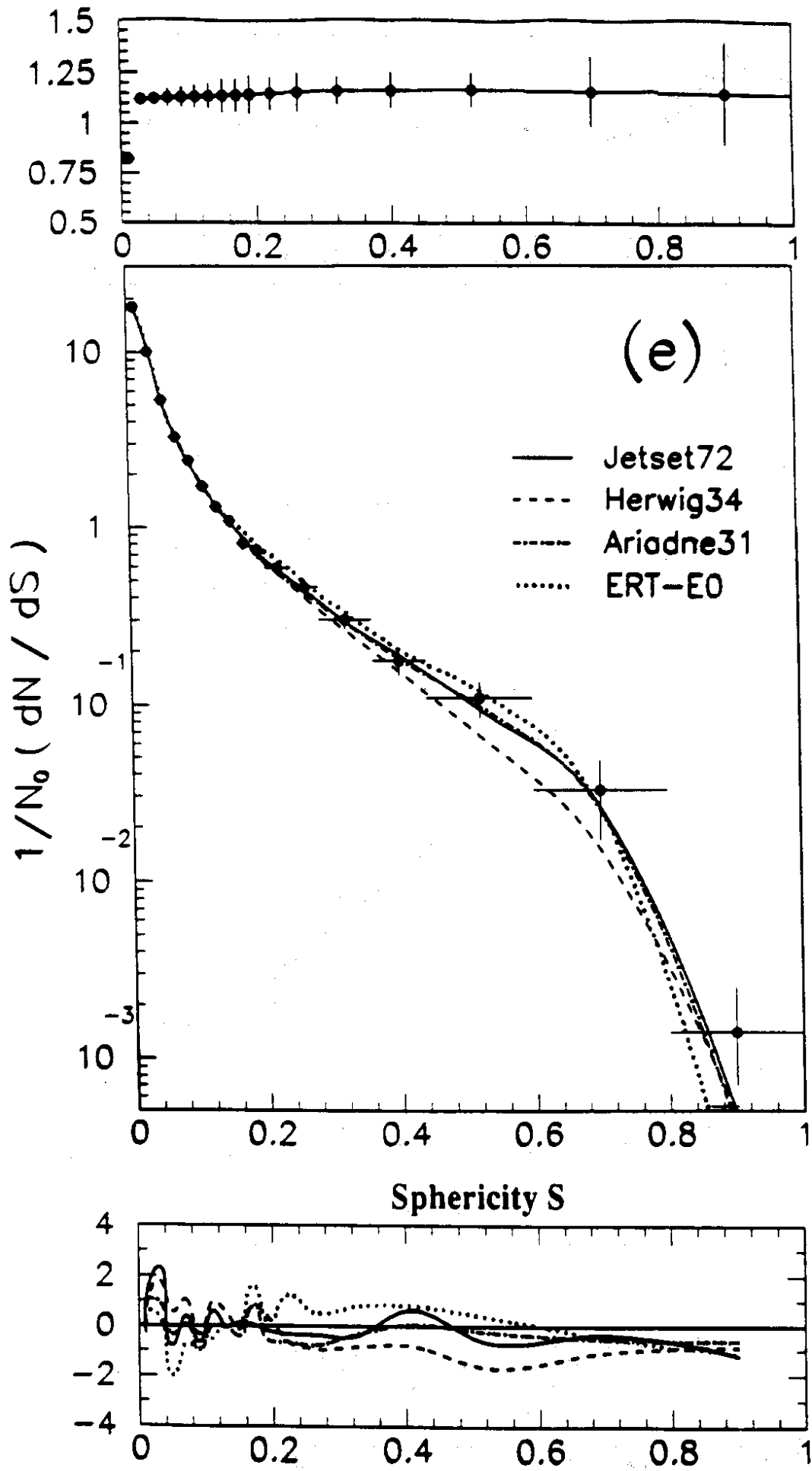


Figure 2

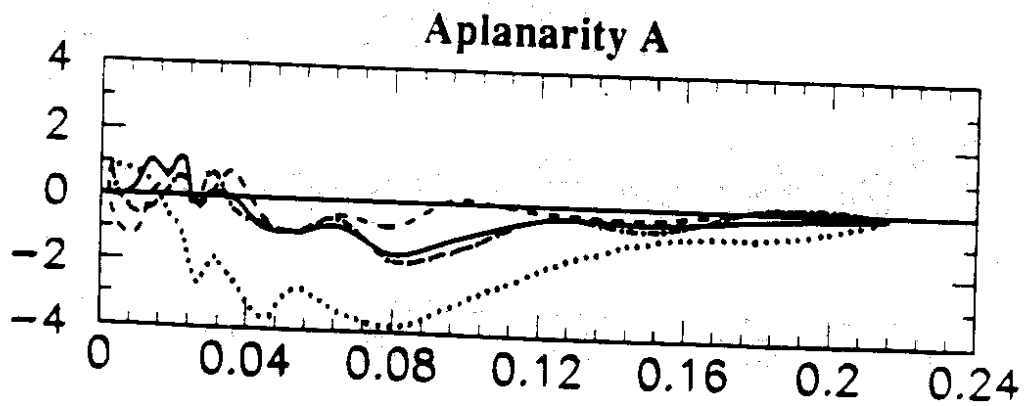
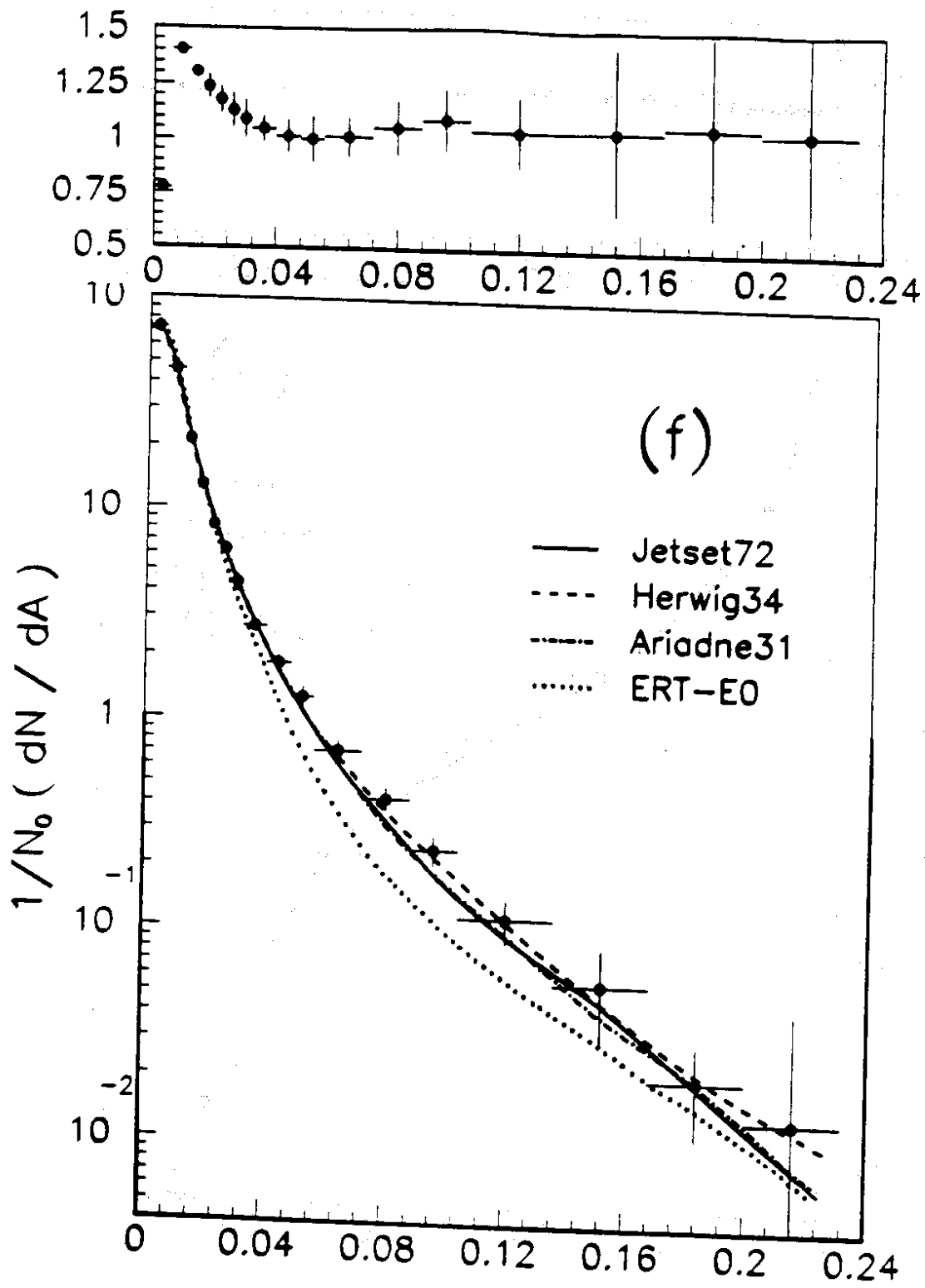


Figure 2

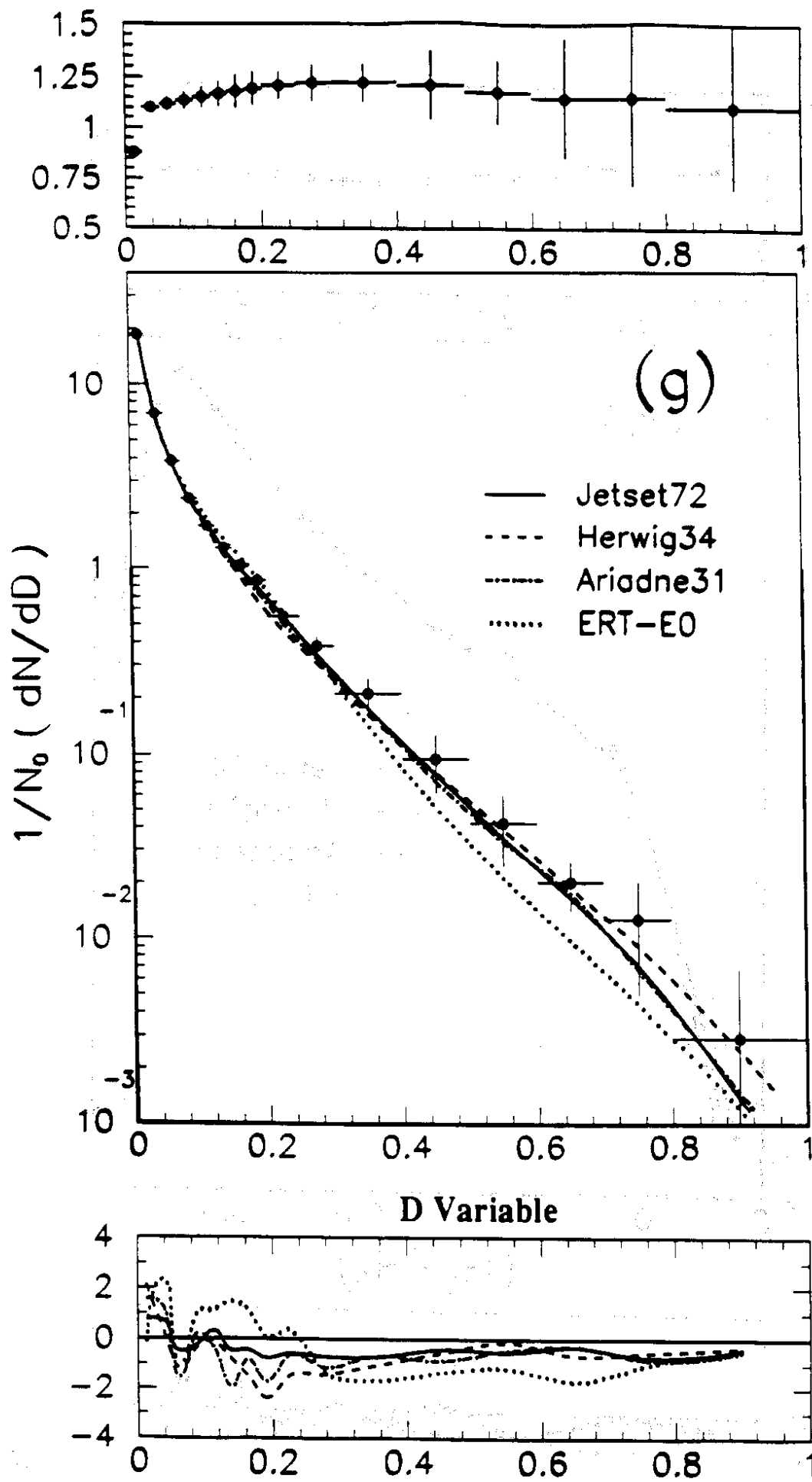


Figure 2

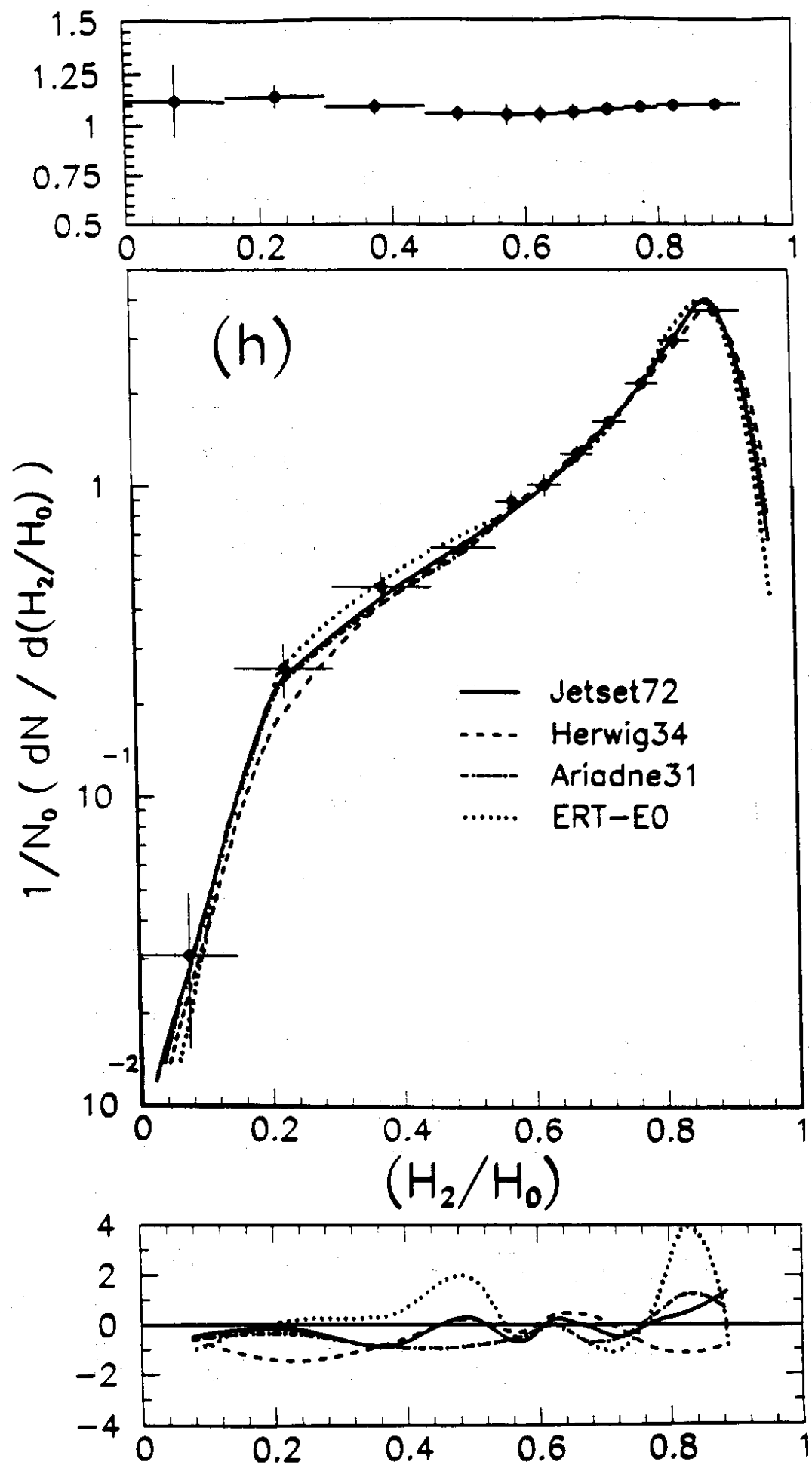


Figure 2

Figure 3

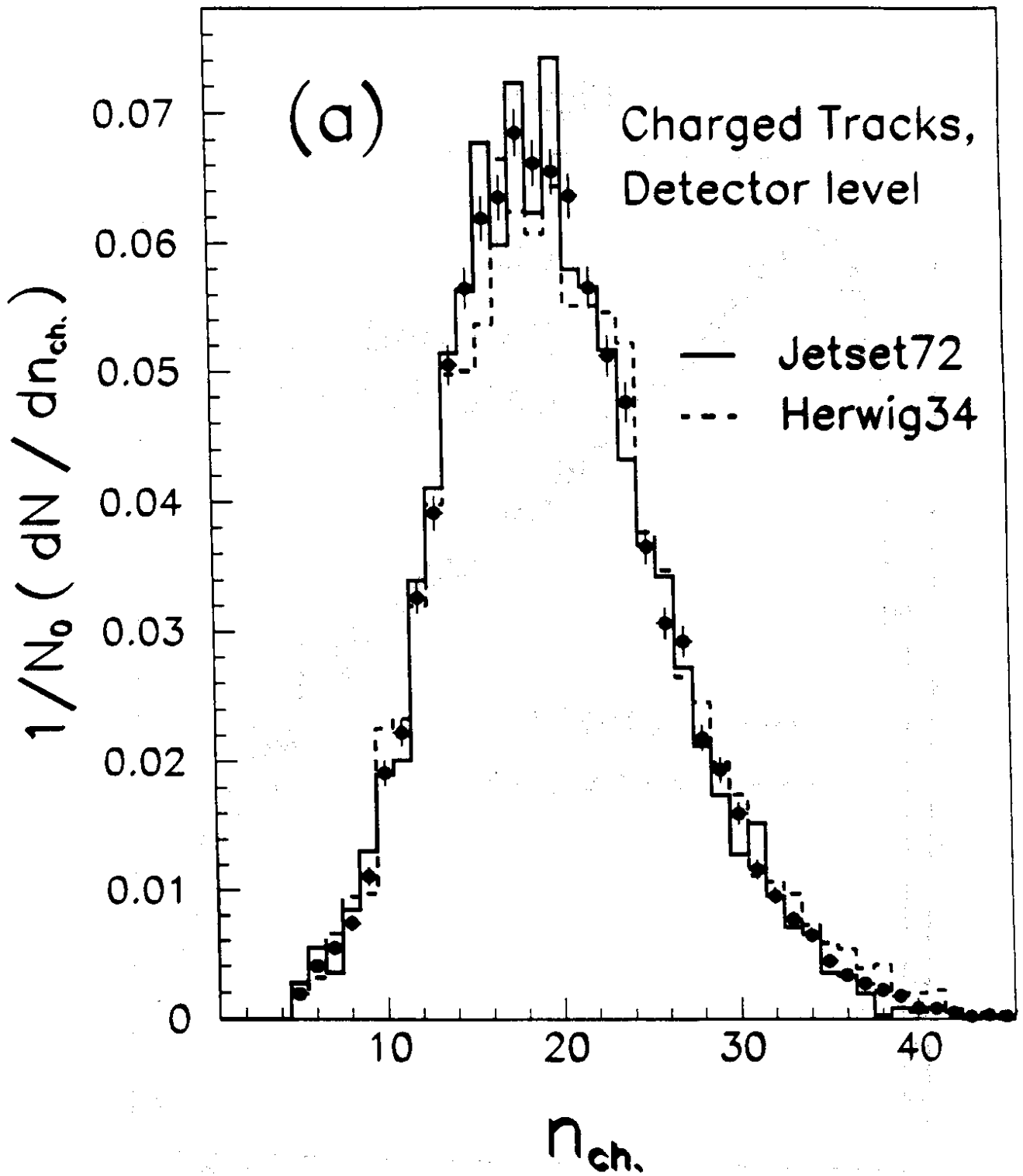




Figure 3

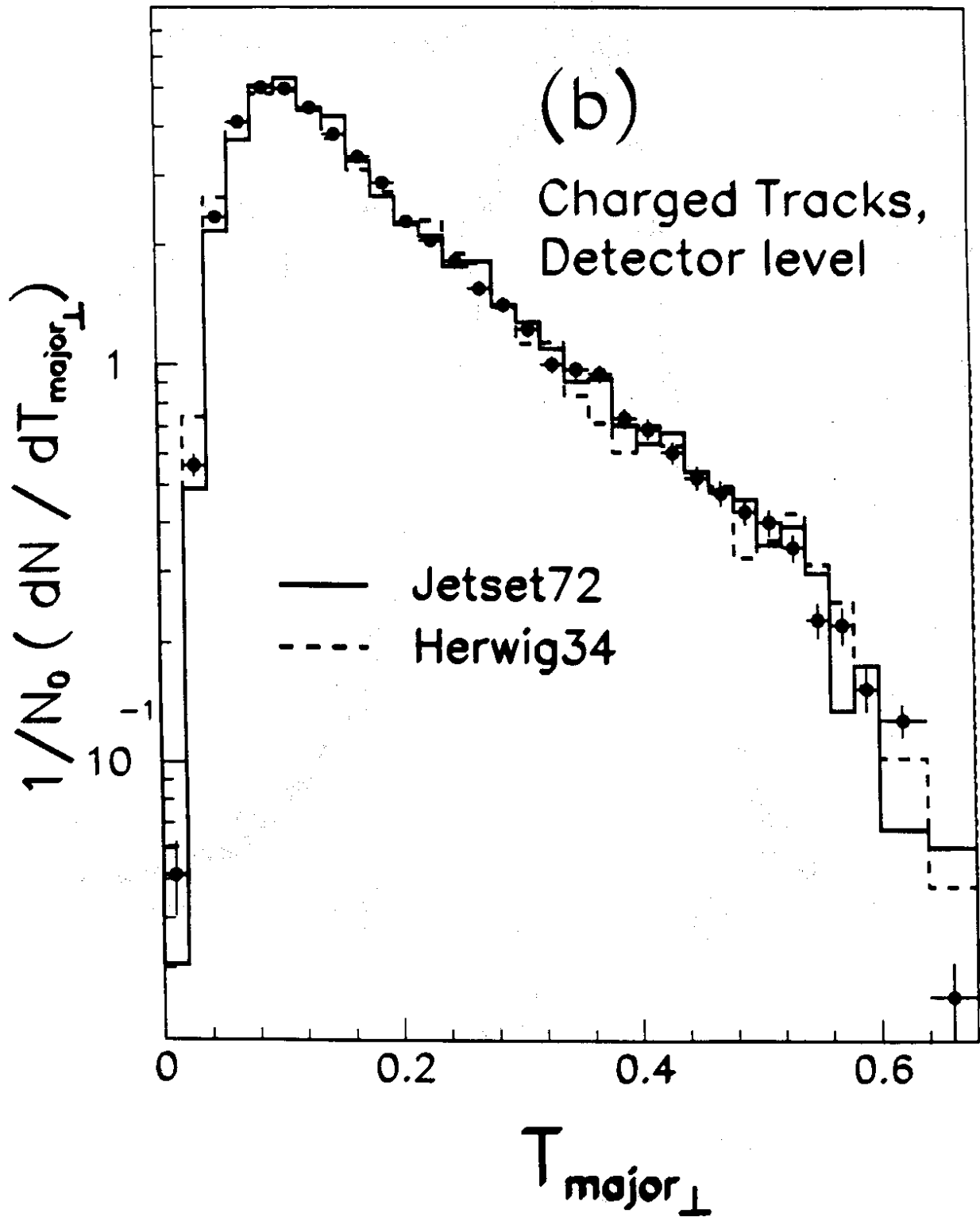


Figure 3

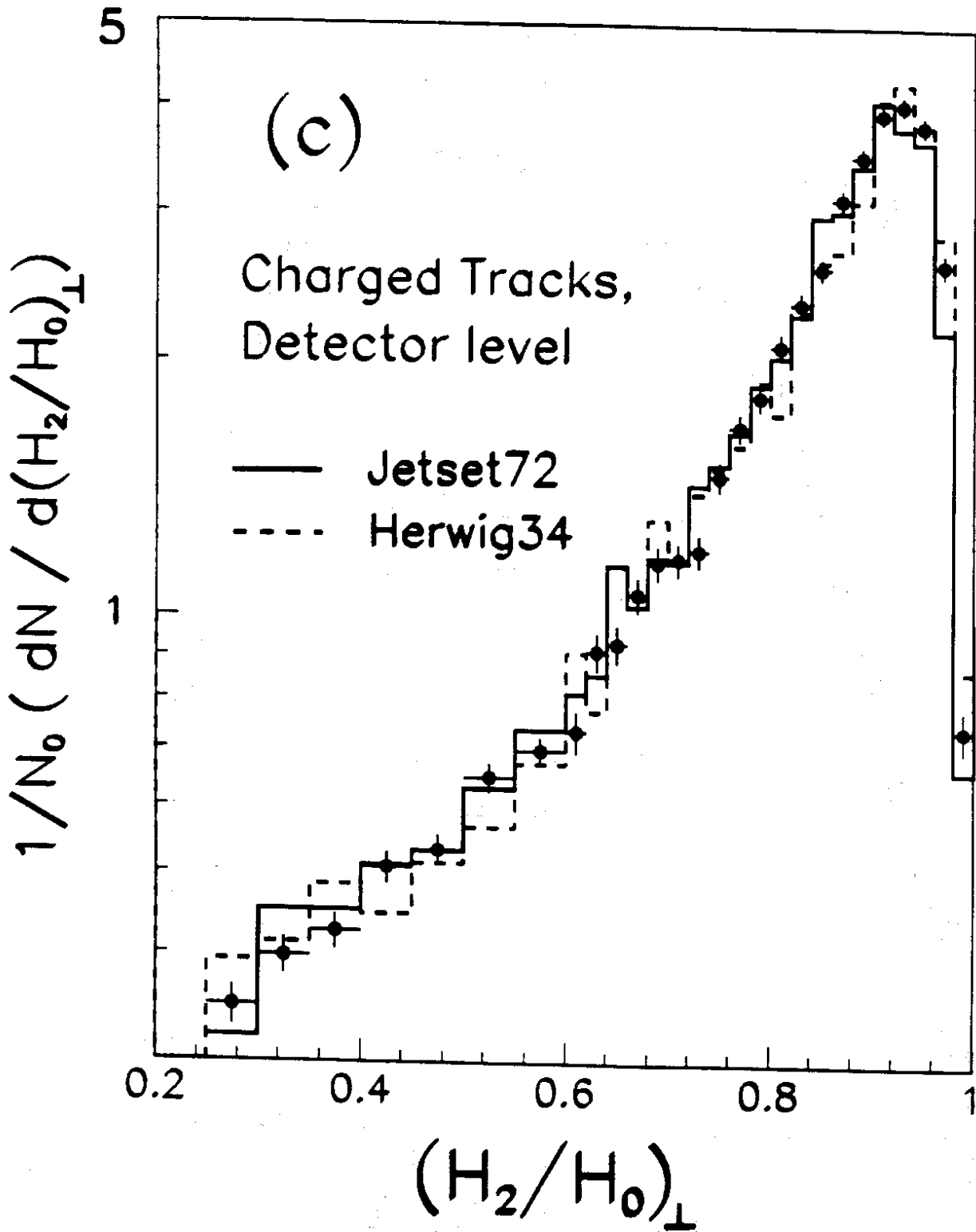


Figure 3

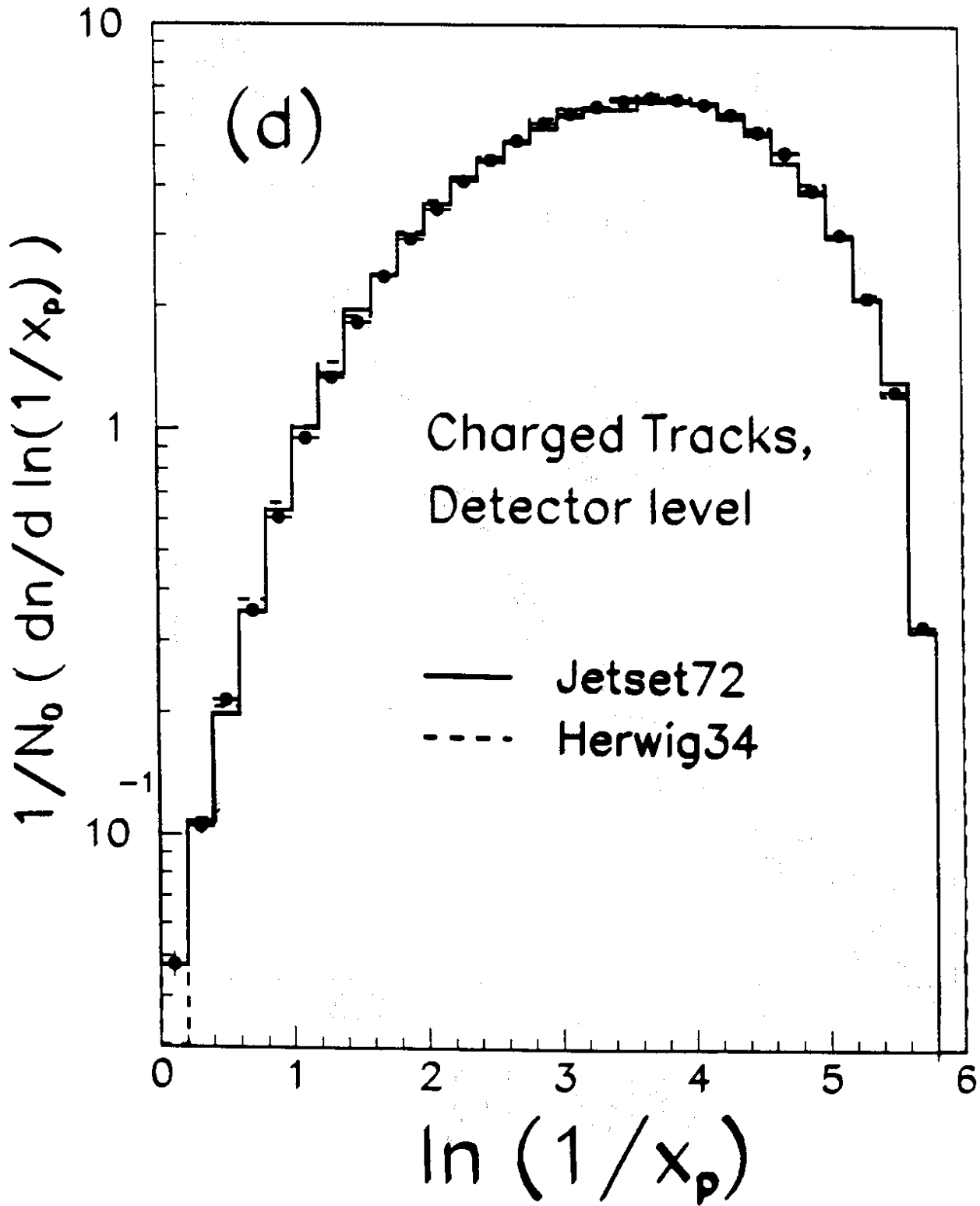


Figure 4

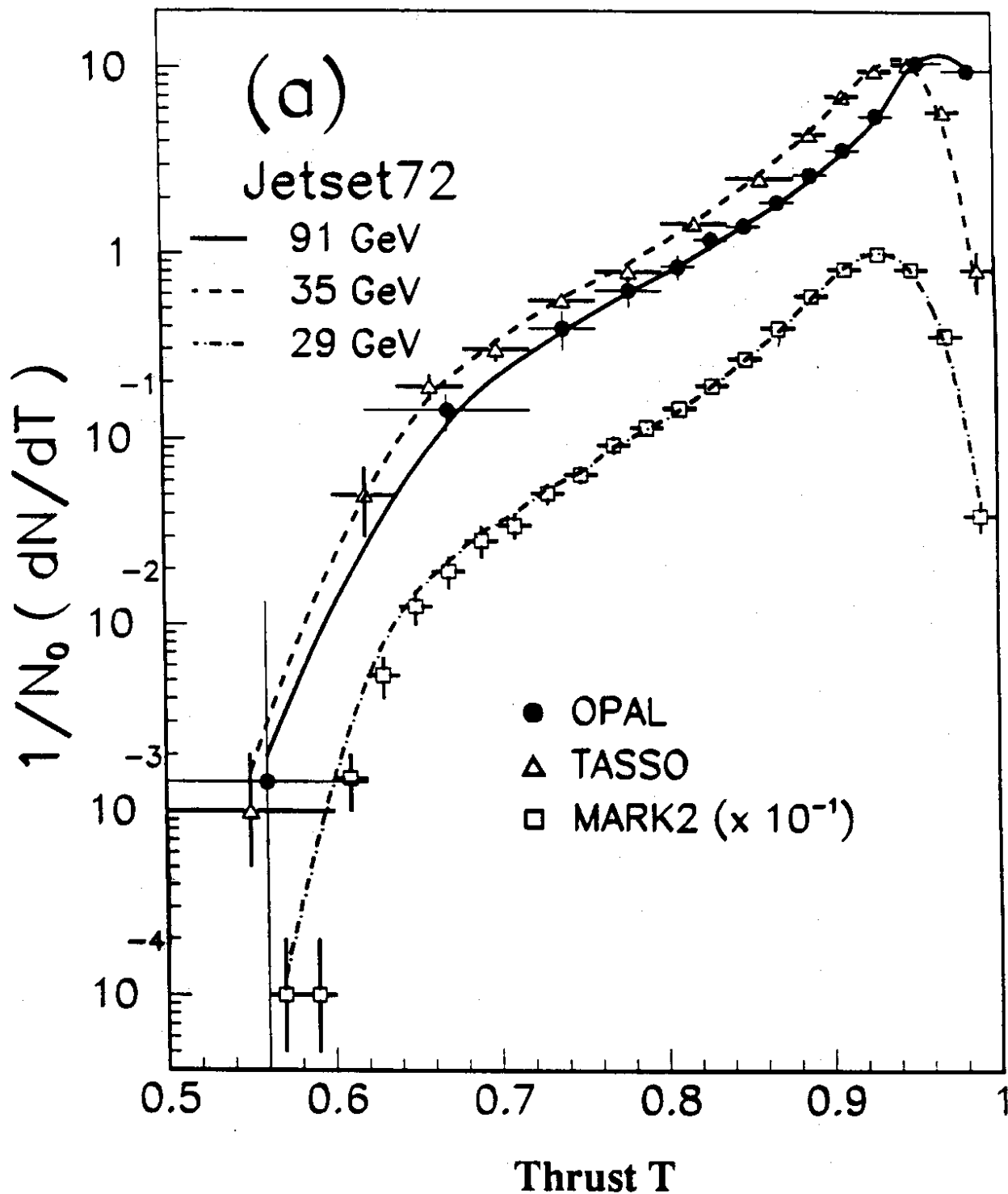


Figure 4

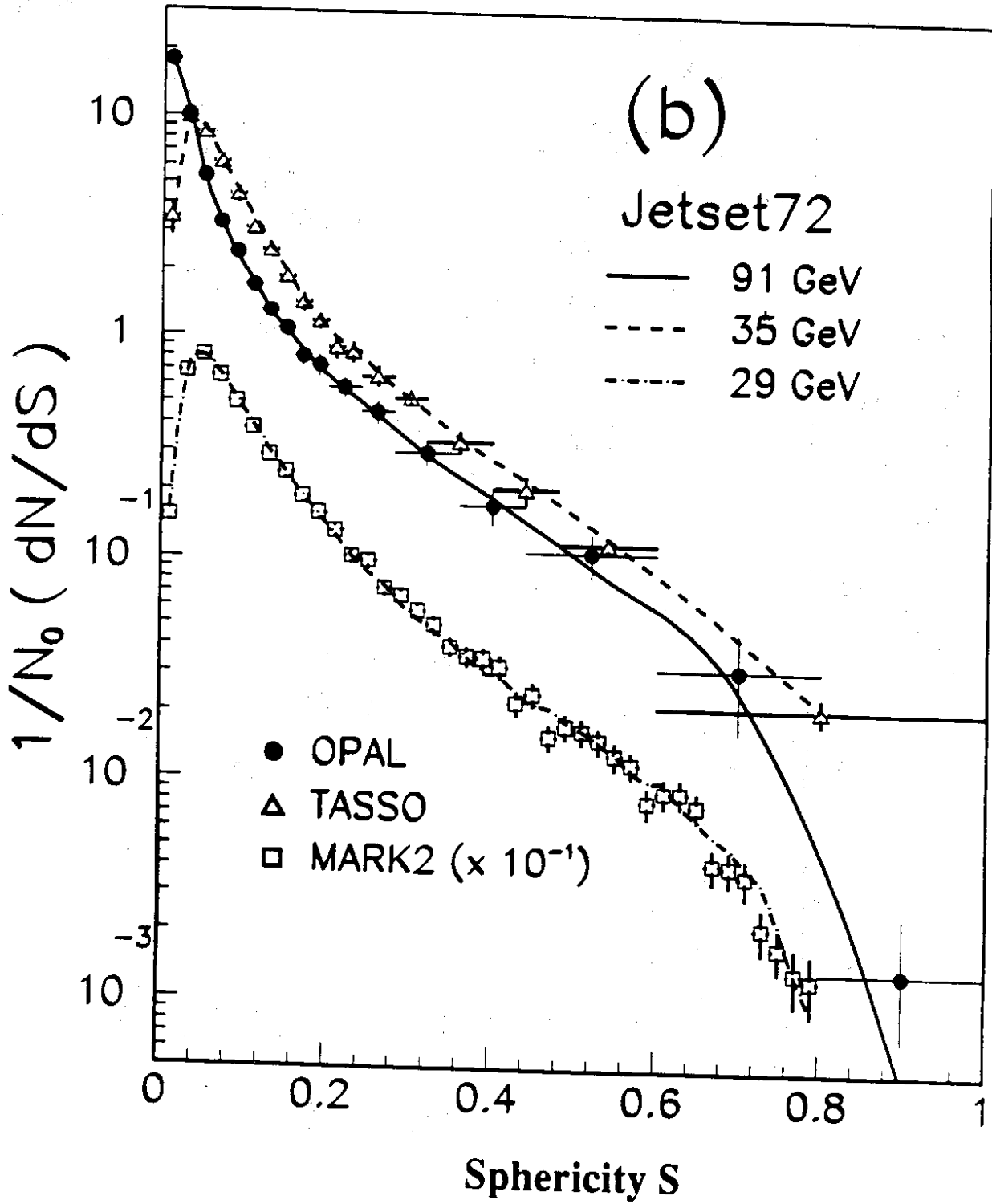


Figure 4

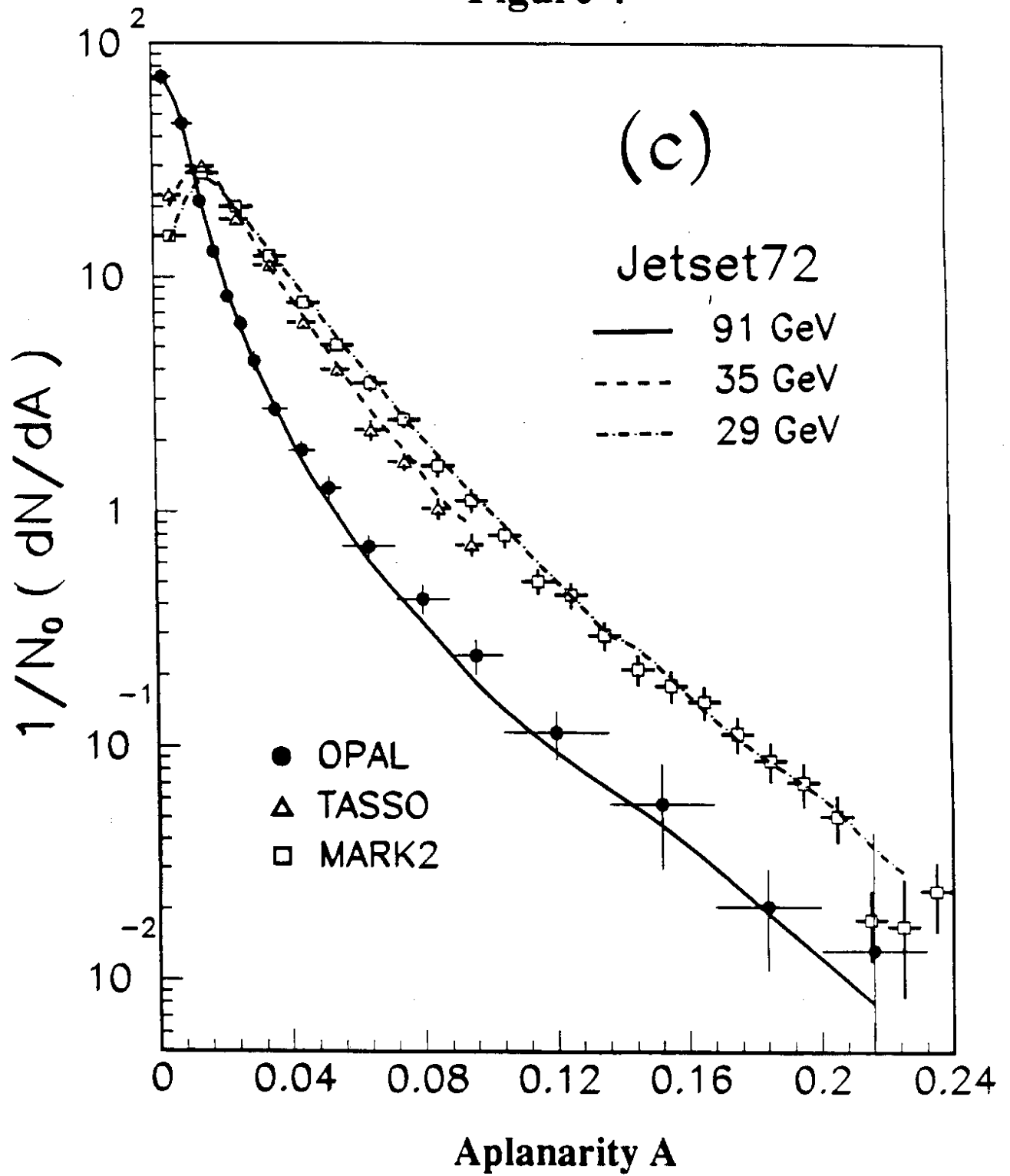


Figure 5

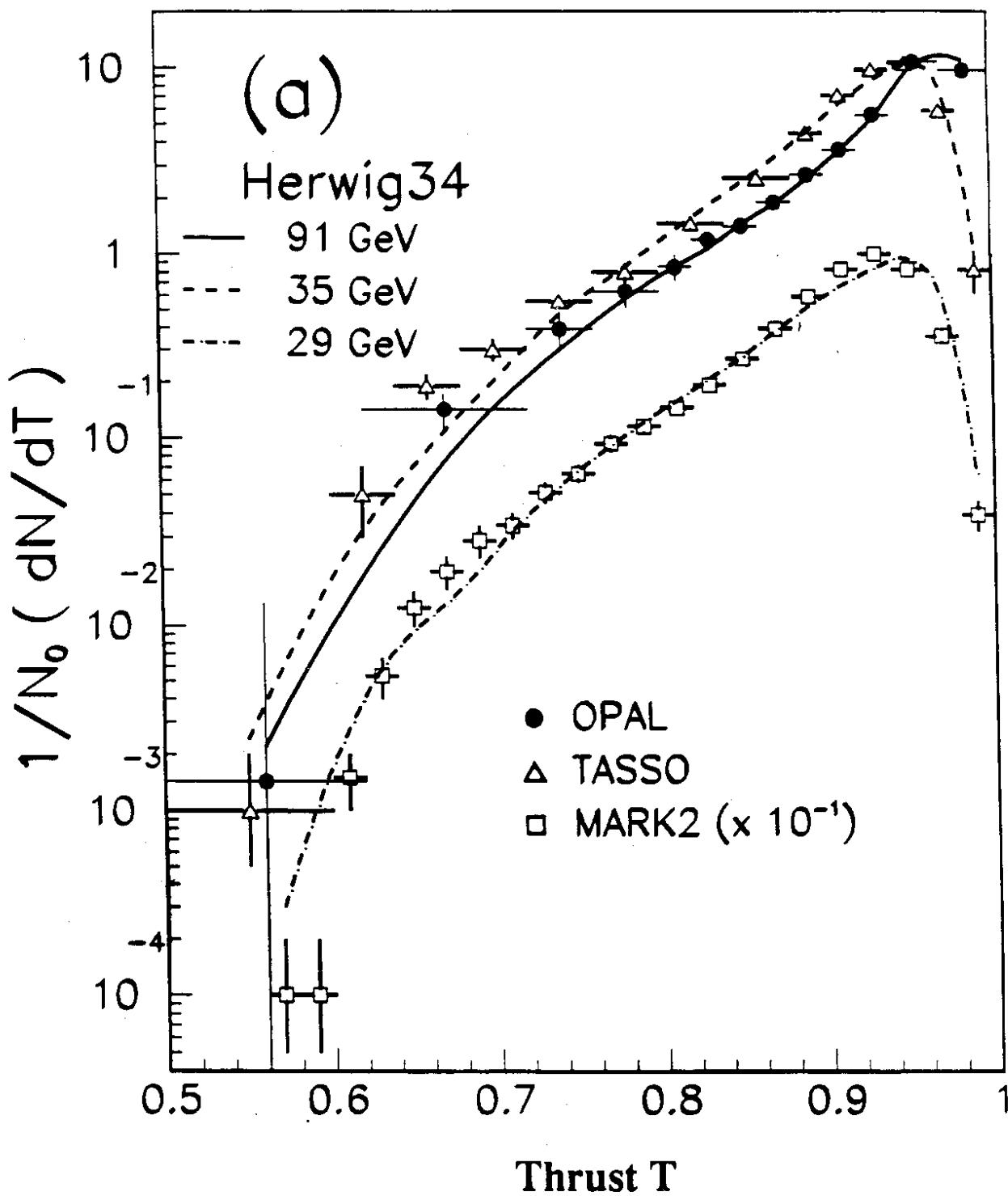


Figure 5

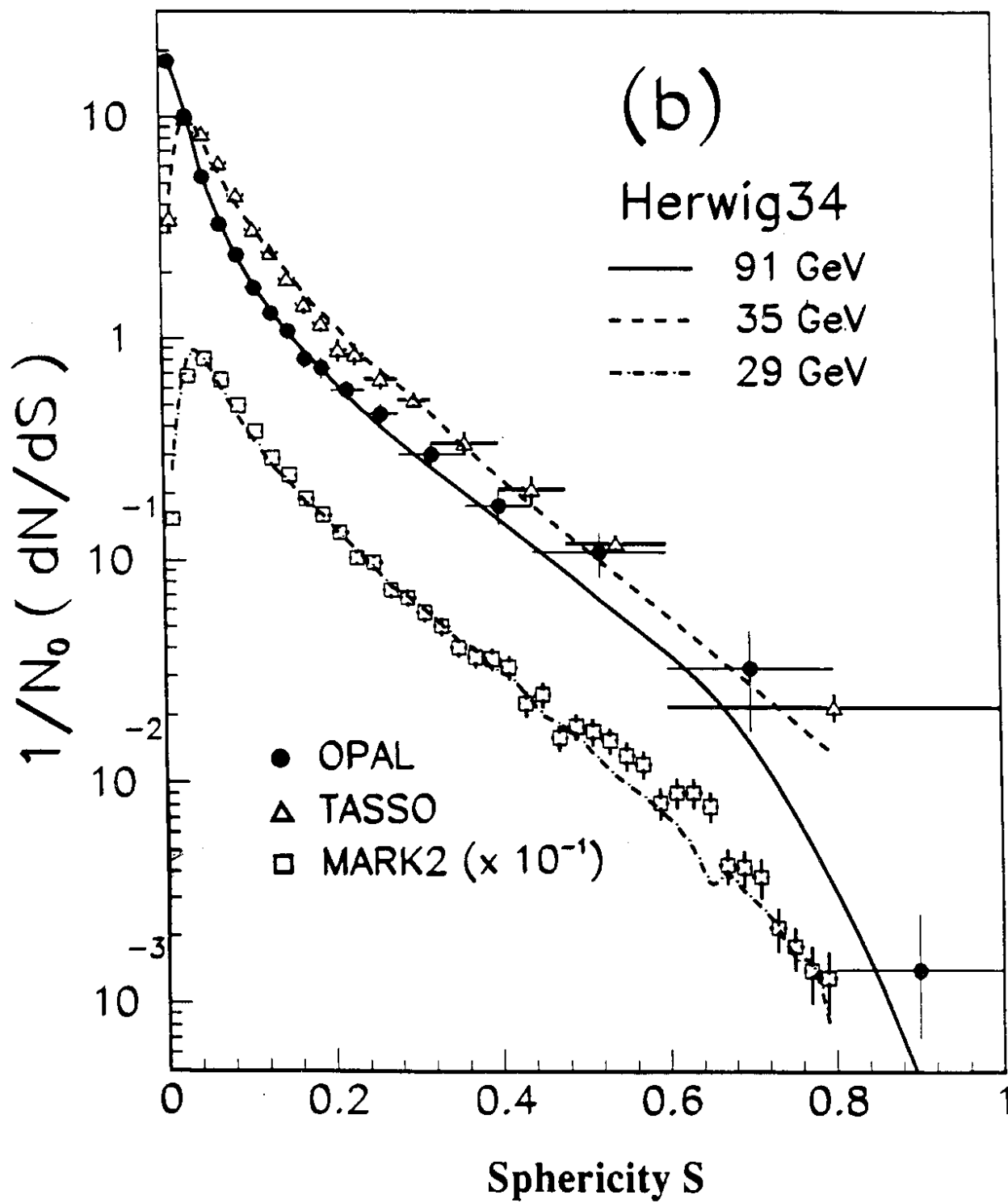




Figure 5

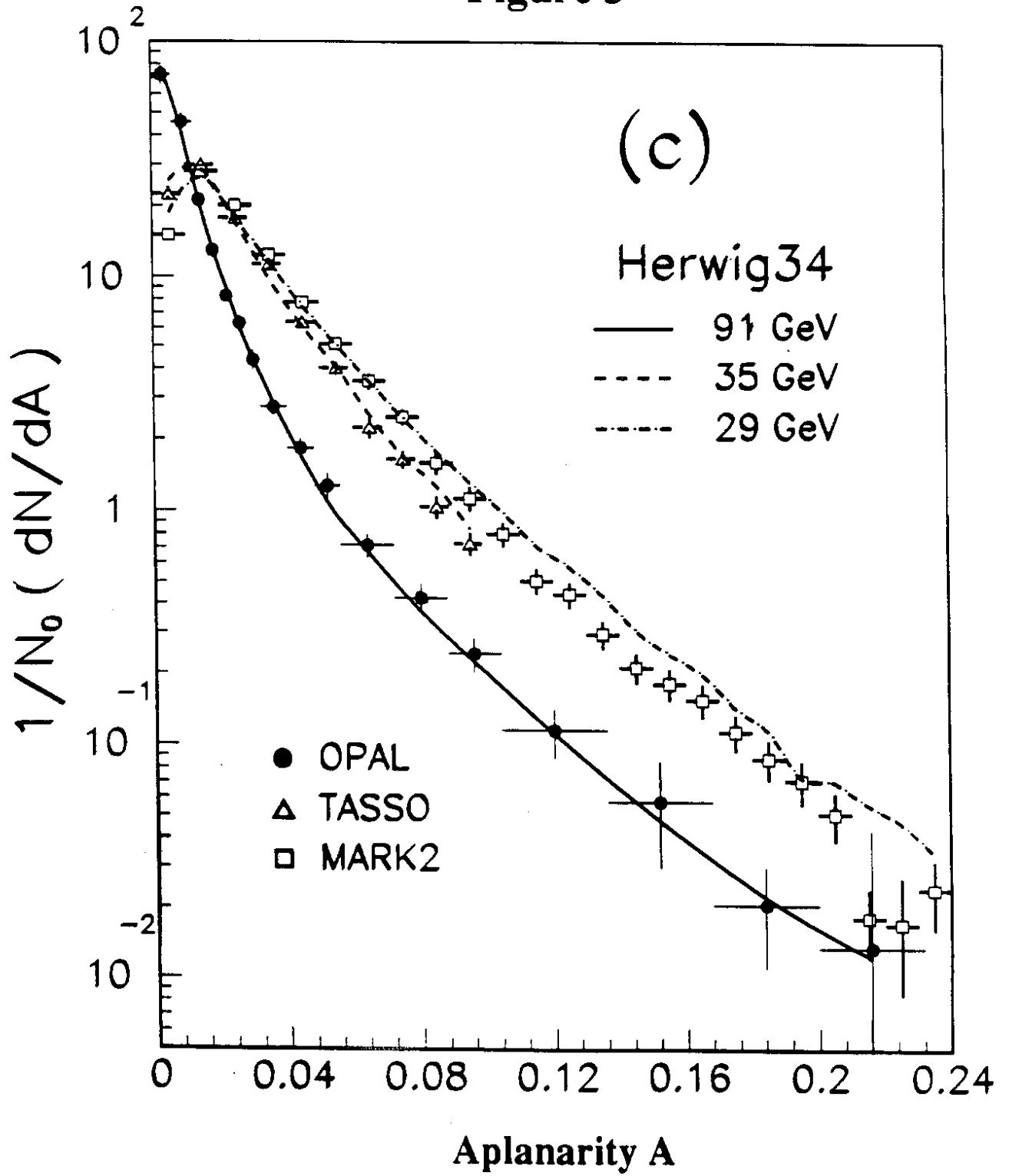


Figure 6

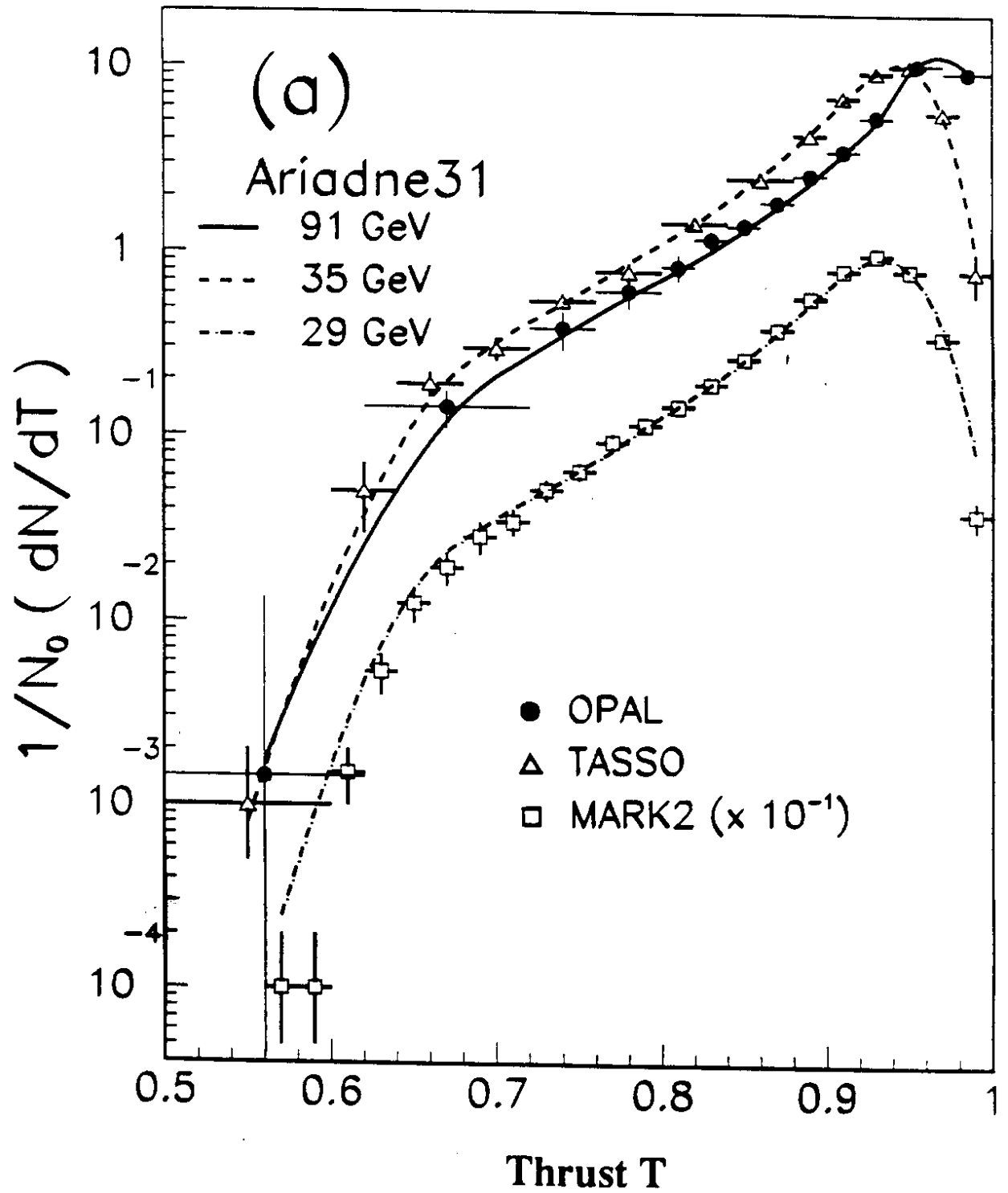


Figure 6

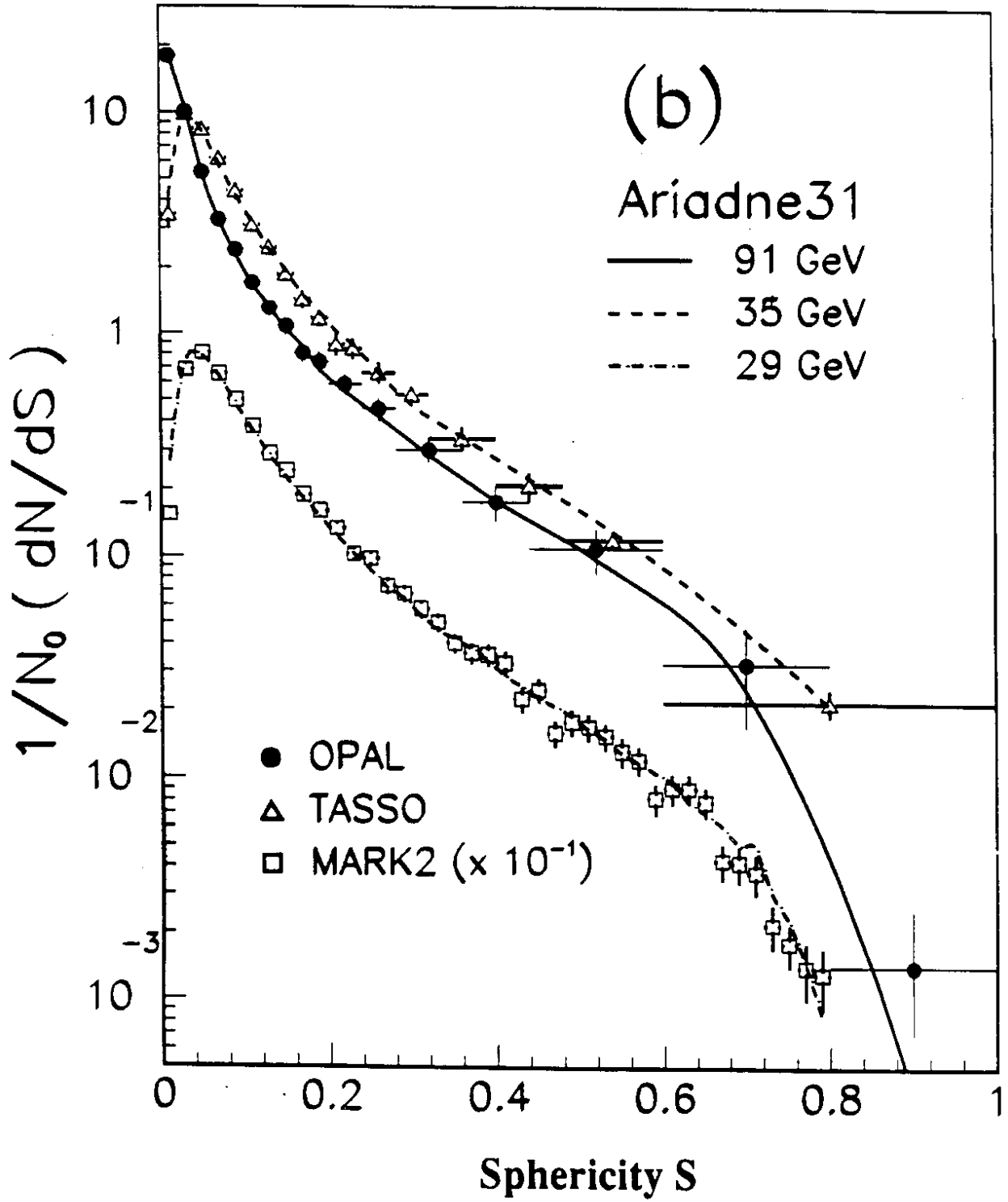


Figure 6

